Cracking behavior of segmented-casting joint in steel-UHPC composite bridge deck system

Experiment and numerical simulation

Su, Qingtian; Xie, Wei; Shi, Zhanchong; Chen, Debao; Hendriks, Max

DOI
10.1016/j.engstruct.2024.118457

Publication date
2024

Document Version
Final published version

Published in
Engineering Structures

Engineering Structures 315 (2024) 118457

Contents lists available at ScienceDirect

Engineering Structures

journal homepage: www.elsevier.com/locate/engstruct

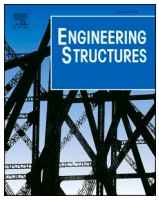

Cracking behavior of segmented-casting joint in steel-UHPC composite bridge deck system: Experiment and numerical simulation

Qingtian Su [a,b], Wei Xie [a], Zhanchong Shi [c,*], Debao Chen [d], Max Hendriks [c,e]

[a] Department of Bridge Engineering, Tongji University, Shanghai 200092, China
[b] Shanghai Engineering Research Center of High Performance Composite Bridges, Shanghai 200092, China
[c] Department of Structural Engineering, Norwegian University of Science and Technology, Richard Birkelandsvei 1A, 7034 Trondheim, Norway
[d] Department of Civil and Earth Resources Engineering, Kyoto University, Kyoto 615-8540, Japan
[e] Department of Engineering Structures, Delft University of Technology, 2628CN Delft, the Netherlands

ARTICLE INFO

Keywords:
Composite bridge deck
UHPC joint
Interface modelling
Cohesive zone model
Cracking behavior

ABSTRACT

The cracking of the pre-/post-casting UHPC joint in the steel-UHPC composite bridge deck system can lead to continuous tensile damage in the UHPC layer, reducing its ability to stiffen the steel deck. This study aims to clarify the cracking mechanism of the segmented-casting UHPC joint, and to provide design recommendations for cracking control. Axial tension tests on full-scale composite deck specimens were conducted, in which the influence of with and without joint, and varying reinforcement ratios on cracking response were identified. Moreover, the nonlinear numerical model for the composite deck, where the UHPC-UHPC interface was simulated in three methods, i.e. unbonded case, cohesive zone model (CZM), and perfectly bonded case, was developed and validated to simulate the crack initiation and propagation of the UHPC layer. Based on the validated numerical model incorporating CZM, improving the bond strength of CZM is more effective in controlling crack opening at the interface than increasing the failure displacement. Finally, optimized reinforcement arrangement and joint shape recommendations were provided to enhance construction convenience, minimize stress concentration, and limit crack opening.

1. Introduction

Compared with the concrete bridge deck slabs, orthotropic steel decks (OSDs) have become t he standard components of most major steel bridges throughout the world, especially for cable-stayed bridges and suspension bridges, owing to their higher load-bearing capacity, lighter weight, longer service life, and easier installation [1]. The OSD is usually overlaid with a thin layer of asphalt wearing course, with a thickness ranging typically from 35 to 80 mm[2]. However, this deck system has been subjected to severe durability problems: fatigue cracking at the OSD [3–5] and wearing of asphalt surfacing [3,5,6]. Fatigue cracking and failure are prominent for the OSD with closed ribs compared to that with open ribs, especially at the rib-to-deck welds which are subjected to secondary out-of-plane deformations and stresses, at the field splicing of ribs with improper welding techniques, and the rib-to-cross-beam intersection with unsuitable details [3]. Cracking and debonding of the asphalt surfacing are directly related to the local flexibility of the OSD, which is featured by the superposed effects of the differential deflections between the deck ribs and the local bending moments under the directly imposed wheel loads[3], and the insufficient bond properties between the deck plate and the bituminous overlay [7].

To address the two main issues of the OSD system, a composite deck system composed of the OSD and a thin layer (35–80 mm) of rebar-reinforced ultra-high performance concrete (UHPC), is proposed [8,9], as shown in Fig. 1. UHPC is a new generation of fiber-reinforced cementitious composites, with exceptional mechanical properties (including elastic modulus, compressive strength, and post-cracking tensile strength), and enhanced durability, compared to normal concrete [10]. Recently, UHPC with significantly improved tensile strain capacity (3–6 %) and crack resistance (a fine crack width of 67–81 μm at the ultimate tensile strain) has been developed [11,12]. For one thing, the welded stud connectors at the OSD/UHPC interface provide a robust connection for the two components, significantly enhancing the local deck stiffness, and thus alleviating the stress of OSD under local wheel loads [13]. For another, the UHPC layer exhibits significantly better bond properties with the bituminous wearing course than the steel deck

* Correspondence to: Richard Birkelandsvei 1A, 7034 Trondheim, Norway.
E-mail address: szc1992czs@163.com (Z. Shi).

https://doi.org/10.1016/j.engstruct.2024.118457
Received 9 April 2024; Received in revised form 5 June 2024; Accepted 16 June 2024
Available online 25 June 2024

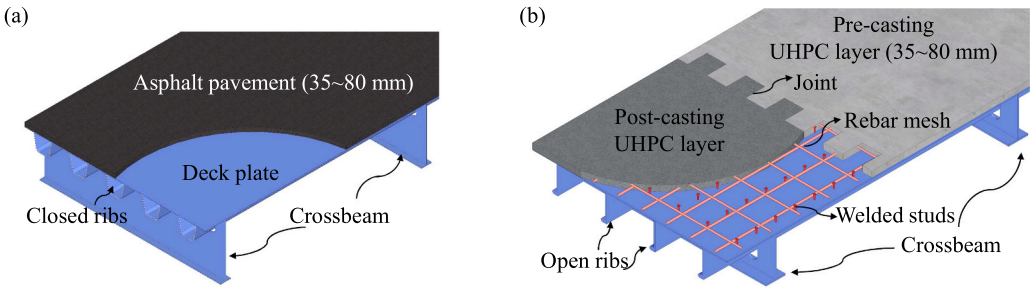

Fig. 1. Bridge deck system: (a) conventional closed-rib OSD system; and (b) open-rib steel-UHPC composite deck system with pre/post-casting UHPC joint.

plate [7], mitigating the wearing course debonding. Owing to the stiffening effect of the UHPC layer, the local wheel loads are sufficiently distributed in the transverse direction. Therefore, the open longitudinal ribs can be introduced in the composite deck system to replace the closed ribs (see Fig. 1(b)), thus reducing the excessive stress concentration, and have been successfully applied in the Dongting Lake Second Bridge[7,14] and Songpu Bridge[15] in China.

The most used construction technology for the steel-UHPC composite deck system at present, mainly consists of three stages: the fabrication of the OSD, the welding of stud connectors (companied with rebar mesh arrangement), and the casting of UHPC layers. Due to the lower production volume of UHPC each time and the larger required paving area, it is inevitable to cast UHPC in stages, thus introducing segmented joints at the pre-/post-casting UHPC layers. Due to the discontinuity of both the UHPC matrix and steel fibers at the joint interface, the UHPC joint is more susceptible to tensile cracking compared to the continuous cast UHPC layer. Hence, the tensile and cracking behavior of UHPC joint has become a major concern over the last decade.

Currently, investigation on the tensile behavior of the UHPC joint is mainly at the interface level [16–18] and the UHPC deck slab level [19–22]. The unified qualitative conclusions, that increasing the interface roughness is beneficial to improving the cracking or bond strength, and enhancing the reinforcement ratio contributes to limiting the interface crack opening, have been drawn. The exploration regarding the tensile and cracking behaviors of UHPC joint at the composite deck system is still limited. Pan et al. [7] performed axial tension and flexural tension tests for the composite deck system with varying-shaped UHPC joint, and proposed the durability-based allowable UHPC tensile stress. Zhao et al. [23] conducted full-scale test and finite-element-based parameter analysis for the flexural response of the composite deck system with dovetail-shaped UHPC joint, and recommended the optimized design values for reinforcement ratio and inclined angle. Chen et al. [24] suggested adopting a high-pressure water jet to rough fine aggregate at the UHPC joint compared with manual roughing and epoxy resin. In summary, the above investigated UHPC joints in the composite deck system are featured by complicated shapes, which are not conducive to the interface cracking control and joint construction. By comparison, the rectangular joint has a relatively simple shape which is beneficial for joint stress transferring as well as field construction, thus has been suggested by the design recommendation for the composite deck system [25].

The composite deck system has been extensively used as the deck component in steel box girder or steel truss for highway bridges in China. Under the first system of the bridge structure, the composite deck system serves as the upper flange of the box girder or the truss girder and is subjected to approximately direct tension in the negative bending moment zone. However, insight into the whole tensile failure process and cracking response of the composite deck system with rectangular UHPC joint in direct tension, is still lacking. Moreover, an appropriate numerical method to accurately predict the crack opening development at the joint interface, is to be developed and validated. The principal parameters, such as the interface bond properties which are associate with interface-finishing techniques, the reinforcement arrangements, and the joint shapes which determine the initiation of interface cracks, governing the crack opening control at the UHPC joint, are to be further quantified.

Table 1
Specimen design.

No.	Casting process	Joint	Rebar quantity	Reinforcement ratio
SN-1	Continuous	—	6	3.4 %
SN-2	Segmented	200 mm	6	3.4 %
SN-3	Segmented	200 mm	10	5.6 %

This study aims to clarify the cracking behavior and the tensile failure process of the segmented UHPC joint in the steel-UHPC composite deck system. Full-scale axial tension tests for the deck system with/without UHPC joints were conducted and compared. Three interface-simulating methods in finite element models (FEM) were compared and validated against the experimental measurement, to capture the cracking and tensile response of the composite deck system. Finally, a FEM-based parametric study was performed to quantify the governing parameters for interface crack opening, and optimized design recommendations were provided. The research results will help engineers further understand the tensile failure mechanism and cracking resistance of segmented-casting UHPC joint in the composite deck system. At the same time, it also provides new insights into crack opening control for UHPC joint considering the construction convenience as well as the structural durability.

2. Experimental program

2.1. Test design and conduction

2.1.1. Test design

Three full-scale steel-UHPC composite bridge deck specimens were designed, as listed in Table 1. Fig. 2 shows the specimens, which were composed of flat steel plate (thickness of 12 mm) stiffened by bulb flat ribs (thickness of 11 mm), and steel rebar-reinforced UHPC layer (thickness of 60 mm). Both the longitudinal and transverse rebars had a diameter of 16 mm, and the transverse rebars with a UHPC cover of 15 mm were located above the longitudinal ones. The current designed reinforcement ratio of the UHPC layer in the composite deck system usually adopts 3 %– 4 %, therefore, reinforcement ratios of 3.4 % and 5.6 % were investigated in the experiment accompanied by consideration of convenience of construction. For specimens with 3.4 %-reinforcement-ratio, the steel rebar mesh had a spacing of 100 mm at both the longitudinal and transversal directions, while that with 5.6 %-reinforcement-ratio had a spacing of 60 mm. The steel plate was connected with the UHPC layer by the welded stud connectors (longitudinal and transverse spacings of 200 mm), which had a diameter of 13 mm and a height of 40 mm. The investigated parameters were with/without joint and reinforcement ratio. It should be noted that the specimens were designed into the dog-bone shape to facilitate the enforcement of axial

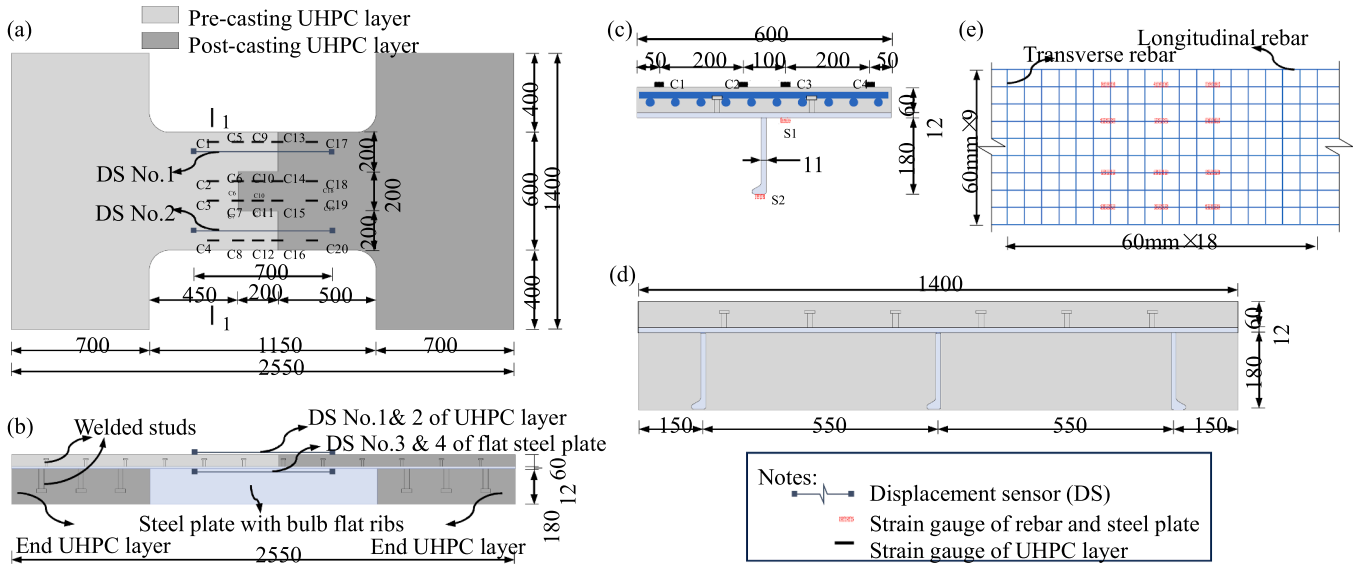

Fig. 2. Specimen design (unit: mm): (a) sizes and strain gauge distribution of UHPC layer with joint; (b) side view and displacement sensor distribution; (c) cross-Sections 1–1; (d) cross-section of the enlarged end; and (e) strain gauge distribution of longitudinal rebar for SN-3.

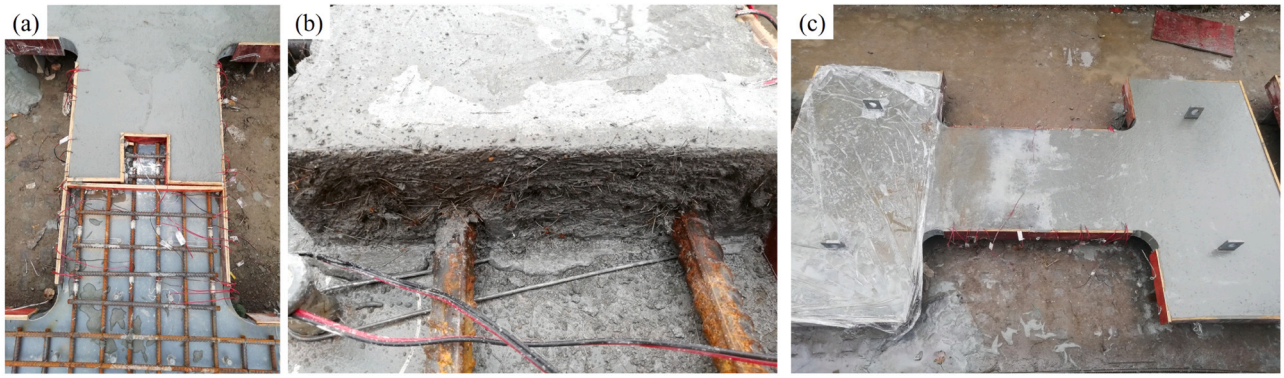

Fig. 3. Main processing procedure of UHPC layer: (a) construction of pre-casting UHPC layer; (b) interface treatment of joint; and (c) construction of post-casting UHPC layer.

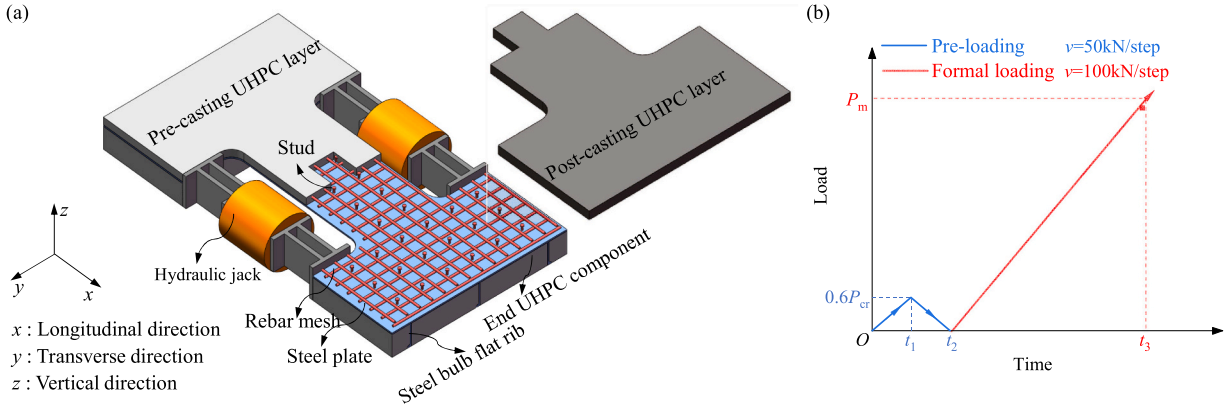

Fig. 4. (a)Test setup and (b) loading protocol.

tensile load through hydraulic jacks. The gaps between the bulb flat ribs at the enlarged two ends were filled with UHPC.

The UHPC layer of specimen SN-1 was continuously cast, while that of specimens SN-2 and SN-3 was composed of the pre-casting and the post-casting UHPC layers. The interface between the pre/post-casting UHPC layer had a size of 200 mm in the longitudinal as well as the transverse directions. As shown in Fig. 3, the pre-casting UHPC layer was first constructed and cured for 24 h, then the formwork of the UHPC layer was removed, and the interface was treated with a wire brush to increase the roughness of the interface and make the steel fibers

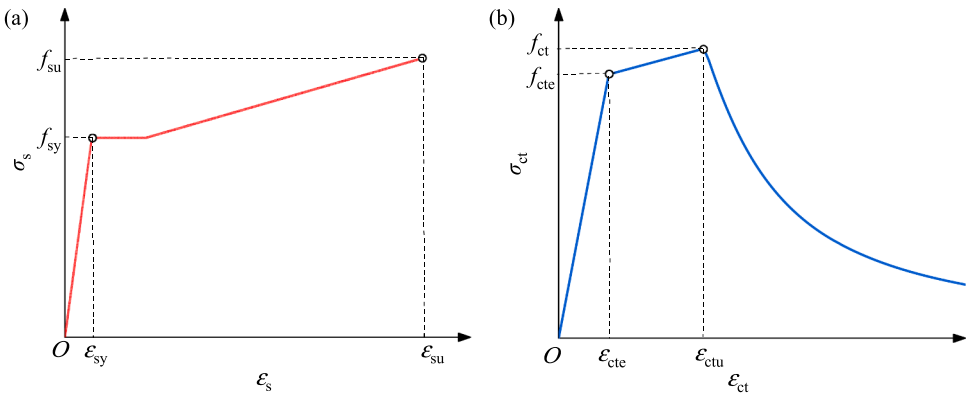

Fig. 5. Simplified tensile stress-strain curves: (a) steel; and (b) UHPC.

Table 2
Basic mechanical properties of steel.

Material	t or d_s [mm]	E_s [MPa]	f_{sy} [MPa]	ε_{sy} [$\times 10^{-6}$]	f_{su} [MPa]
Steel plate	11	227,000	455	2004	608
	12	214,000	411	1921	547
Steel rebar	16	209,000	480	2297	689

Note: t is thickness, d_s is diameter.

Table 3
Mix proportion of UHPC (unit: kg/m^3).

Cement	Silica fume	Fine reactive filler	Quartz Sand	Water	Superplasticizer	Steel fibers
745	223	223	998	179	13	200

uniformly exposed. The post-casting UHPC layer was constructed immediately after the finish of the interface treatment. After the pre- and post-casting UHPC layers were cured for 28 days under natural conditions with an average temperature of 25 °C and an average relative humidity of 75 %, the filled UHPC layer at the enlarged ends was cast. The axial tension test was conducted after the UHPC at the enlarged ends was cured for 28 days.

2.1.2. Test setup and loading protocol

The axial tension test setup is shown in Fig. 4(a). Two hydraulic jacks sharing the same oil source were used to enforce pushing force to the enlarged two ends, and the central part of the specimens was subjected to direct tension. The center of the two hydraulic jacks should be aligned with the centroid of the composite section to prevent the specimen from torsion. As shown in Fig. 2(a) and (b), two displacement sensors with a gauge length of 700 mm were attached to the surface crossing the joint to monitor the longitudinal elongation of the UHPC layer. The corresponding location of the steel plate was also equipped with two displacement sensors to measure the deformation. The strain evolutions of the UHPC interface, continuous UHPC layer, steel plate, bulb flat ribs, and longitudinal rebars were monitored by resistance strain gauges which are distributed as shown in Fig. 2(a), (c) and (e). In addition, the crack width development of the joint interface was detected by a crack observer with an accuracy of 0.01 mm.

Fig. 4(b) shows the loading protocol, which consisted of the pre-loading and formal loading stages. For the pre-loading, the load was enforced to 0.6 times the estimated cracking load of the UHPC layer with loading increments of 50 kN. After the unloading of the pre-loading stage, the actual loading with increments of 100 kN was conducted, and the target load was kept for 5 min to determine the crack localization and to capture the crack opening displacement.

Table 4
Basic mechanical properties of UHPC.

E_c [MPa]	f_c [MPa]	f_{cte} [MPa]	f_{ct} [MPa]	ε_{cte} [$\times 10^{-6}$]	ε_{ctu} [$\times 10^{-6}$]
47,900	127	9.2	10.1	190	3198

Notes: E_c and f_c are the elastic modulus and compressive strength, respectively; f_{cte} and ε_{cte} are the elastic tensile strength and the corresponding strain, respectively; f_{ct} and ε_{ctu} are the tensile strength and the corresponding strain, respectively.

2.1.3. Material properties characterization

The steel plate and rebar used were Q345q, and HRB400, respectively. Based on the uniaxial tension test [26] on steel plate and rebar, the basic mechanical properties, including the elastic modulus E_s, the yielding strength f_{sy}, the tensile strength f_{su}, and the yielding strain ε_{sy} shown in Fig. 5(a), are listed in Table 2. The values are the average numbers obtained from three identical specimens.

Table 3 lists the mix proportion of UHPC, which had a steel fiber volume of 2.5 %. The steel fibers used had a length of 13 mm and a diameter of 0.2 mm (l_f=13 mm, d_s =0.2 mm). The elastic modulus and tensile strength of the steel fibers were 200,000 MPa and 2500 MPa, respectively. The compressive strength test and elastic modulus test for prism specimens with sizes of 100 mm × 100 mm × 300 mm were conducted referring to Chinese Standard CECS13[27]. The axial tension test for dog-bone-shaped specimens according to Ref. [28] was performed. The schematic tensile stress-strain curve of UHPC is plotted in Fig. 5(b), which exhibits strain hardening after the first cracking. The basic mechanical properties of UHPC are summarized in Table 4. The test results were for specimens under the same natural curing conditions as the composite bridge deck specimens for 28 days, and the values were the average for each three samples.

2.2. Test results and analysis

2.2.1. Global tensile response

The axial load-elongation responses of the UHPC layer and the steel plate are shown in Fig. 6. The elongation was the average reading of the two displacement sensors. Due to operational errors, the complete tensile response curve of specimen SN-1 was not obtained, except for the characteristic points, including first cracking and yielding.

As shown, the elongation of the UHPC layer was approximately equal to that of the steel plate during the whole loading process, demonstrating the arrangement of the welded stud connectors provided an effective connection for the two components to ensure the deformation coordination. The global tensile response of the specimens with UHPC joint (SN-2 and SN-3) can be divided into three stages:

I, elastic stage, first-cracking of the UHPC interface (corresponding to P_{cr1}) marks the end of this stage.

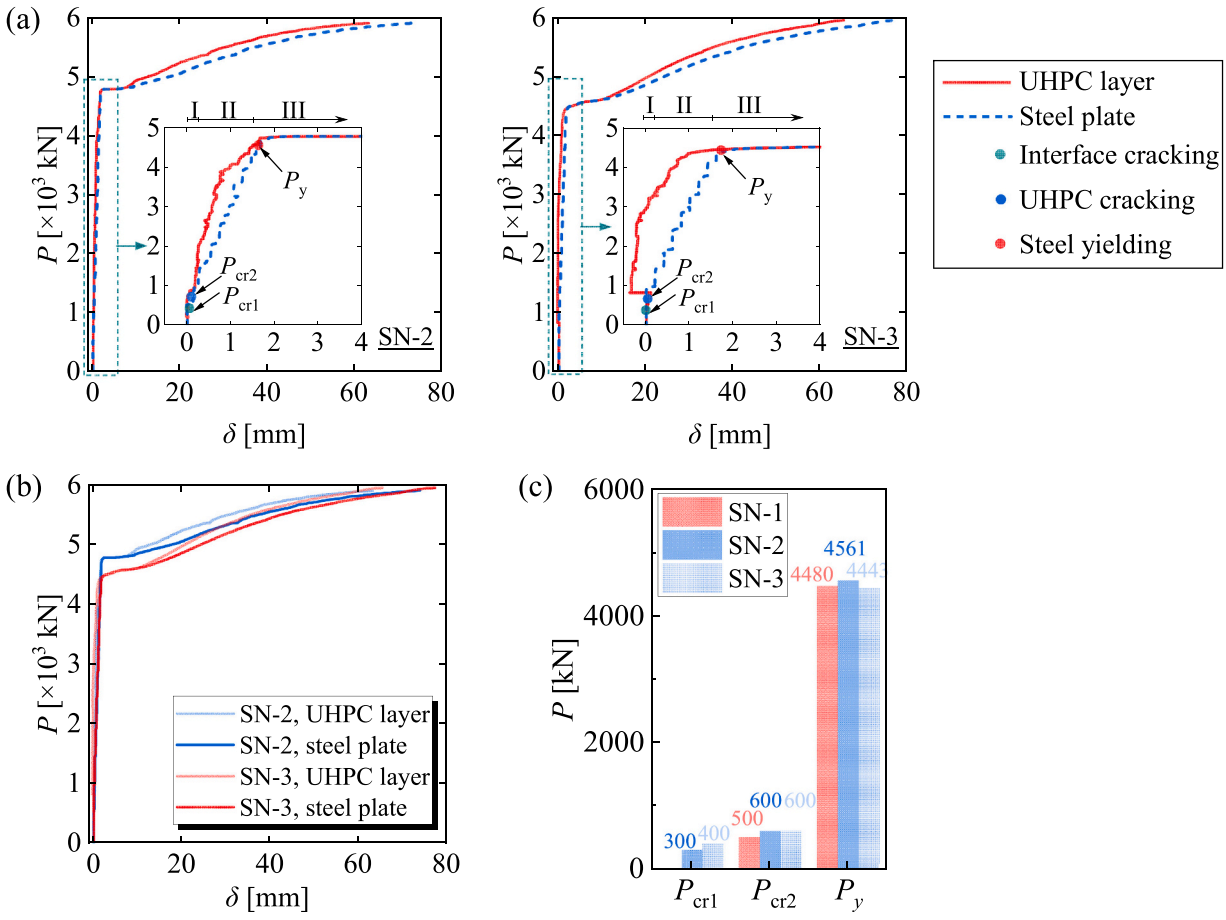

Fig. 6. Axial load-elongation response: (a) SN-2 and SN-3; (b) comparison between SN-2 and SN-3; and (c) comparison of the characteristic loads.

II, multi-cracking stage, the first cracking of the continuous UHPC layer (corresponding to P_{cr2}) emerged after the first cracking of the interface, which originated from the intersection point of longitudinal and transverse edges for the interface. At this stage, the continuous UHPC layers at the pre- and post-casting zones exhibited multiple cracks, which were featured by the thin and dense distribution, owing to the fiber-bridging effect.

III, yielding/crack localization stage, the steel rebar and steel plate yielded (corresponding to P_y) approximately simultaneously because of the uniform direct tension state and the similar yielding strains of the two components. The yielding of rebar was accompanied by the crack localization of several main cracks at the continuous UHPC layers, and the continuous pull-out of the steel fibers from the UHPC matrix and the related widening of crack opening displacements characterized the crack localization. Moreover, the thin cracks (close to the localized crack) developed at stage II became invisible at this stage owing to the squeeze effect induced by the widening of localized cracks. These phenomena are similar to the axial tension response of rebar-reinforced UHPC members in existing studies [29].

Specimen SN-2 was loaded to the fracture of two rebars at one localized crack at the continuous UHPC zone, the loading of specimen SN-3 was terminated prior to the rupture of the rebar. The global tensile response of the specimen without UHPC joint (SN-1) was almost identical to that with UHPC joint (SN-2 and SN-3). It should be noted that, as shown in Fig. 6(a), the axial load-elongation curve of the UHPC layer for SN-3 shifted to the left after the first cracking of the continuous UHPC layer. This could be interpreted by the squeeze influence of the crack developed beyond the gauge length on the measuring point of the displacement sensor.

The axial load-elongation response comparison between specimen SN-2 and SN-3 is shown in Fig. 6(b). Though specimen SN-3 had a larger reinforcement ratio than specimen SN-2, the yielding plateau of specimen SN-3 was located below specimen SN-2. This may be induced by the dispersion of one specimen. A comparison of the characteristic loads for all the specimens is shown in Fig. 6(c). The first cracking load of the interface (P_{cr1}) for specimen SN-2 was smaller than specimen SN-3, indicating increasing the reinforcement ratio is beneficial for increasing the cracking load of the interface. The yielding loads of all the specimens were close to each other. This is because the steel plate predominately determines the load-bearing capacity of the composite deck, which is not significantly influenced by the reinforcement ratio and the UHPC layer (whether it has a joint or not).

2.2.2. *Load-strain response*

Fig. 7(a) shows the axial load-strain response of each component, the UHPC layer, the rebar, and the steel plate. Although the specimens were at direct tension, the strains of each component under the same load had a relatively large difference with the increasing axial load. This could be mainly induced by the crack initiation and development at the interface as well as at the continuous UHPC layer.

The axial load-strain response of the UHPC joint is shown in Fig. 7(b). In general, for the same cross-section location, the tensile strain at the interface developed faster than that at the continuous UHPC zone, indicating the interface is more prone to cracking than the continuous UHPC layer. The tensile strain at the interface can achieve 0.001, this is because the interface at the UHPC surface was covered by the UHPC matrix during the construction of the post-casting UHPC layer.

2.2.3. *Cracking patterns and failure modes*

Fig. 8(a)~(c) show the cracking pattern of the UHPC layer at the end

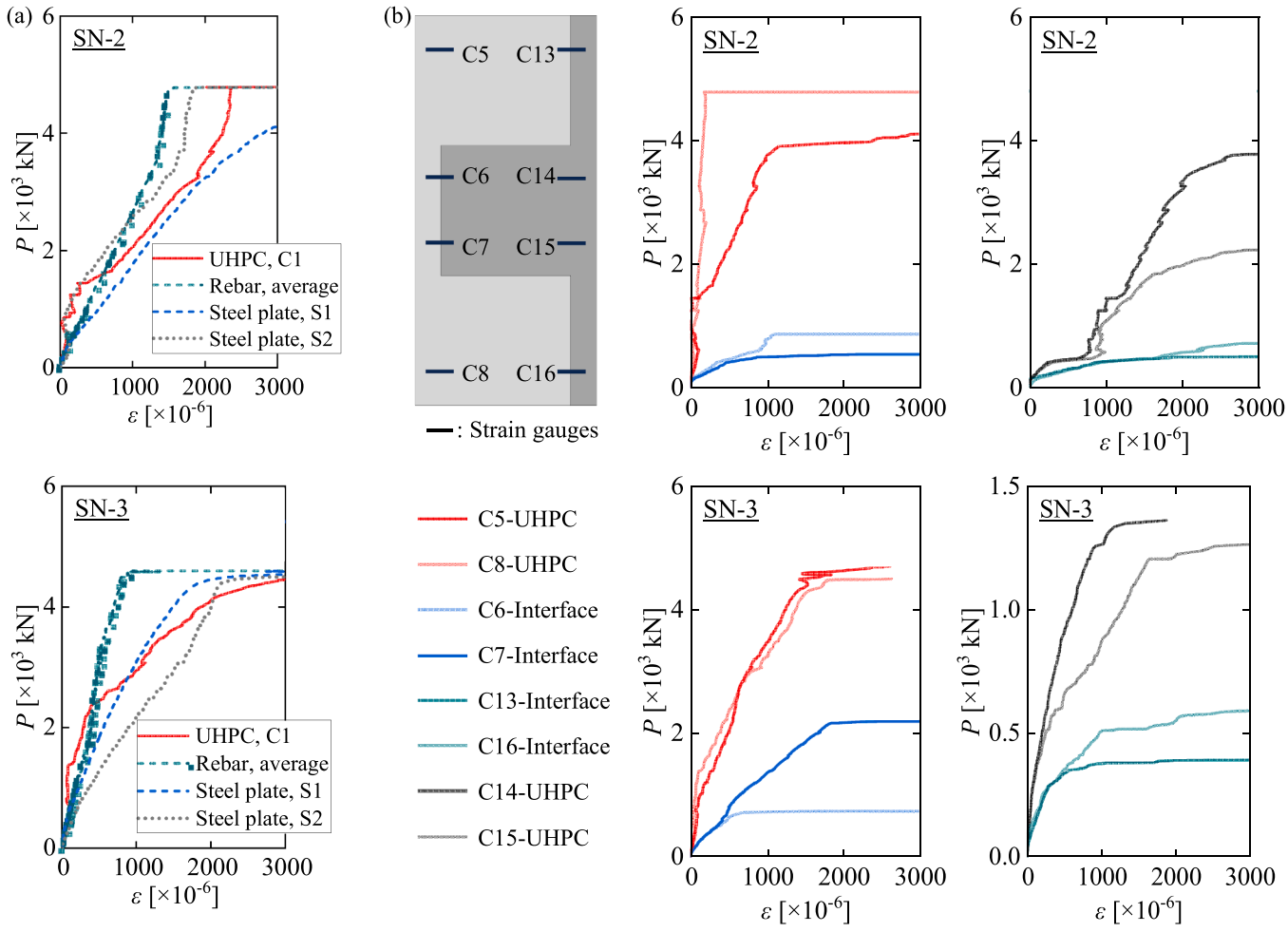

Fig. 7. Axial load-strain response: (a) each component; and (b) UHPC joint.

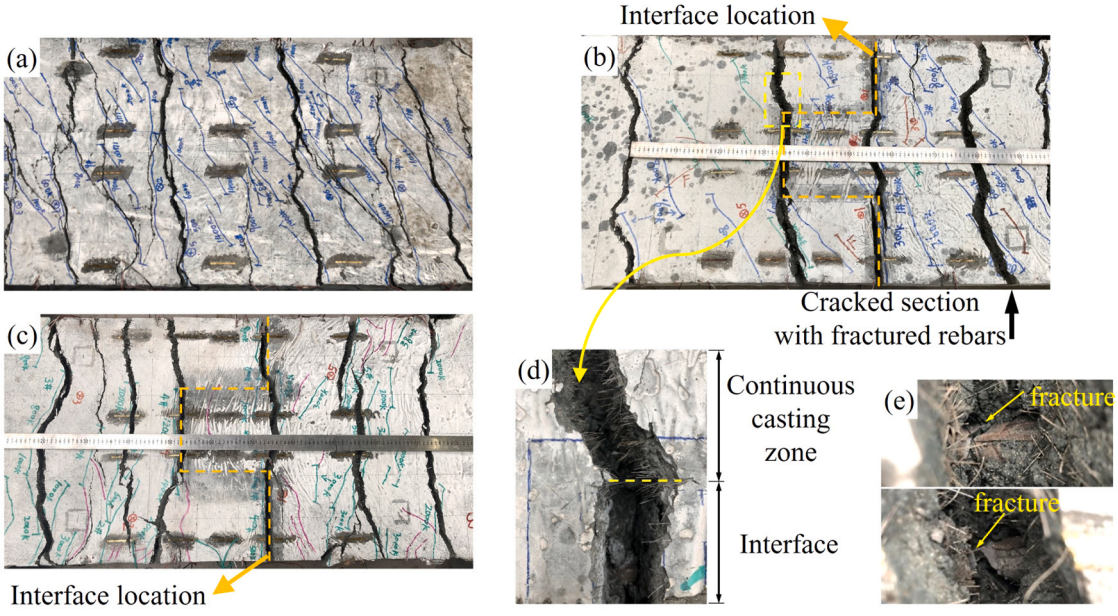

Fig. 8. Cracking patterns and failure modes: (a) SN-1; (b) SN-2; (c) SN-3; (d) fracture surface comparison between continuous UHPC and interface; and (e) fracture of rebars in specimen SN-2.

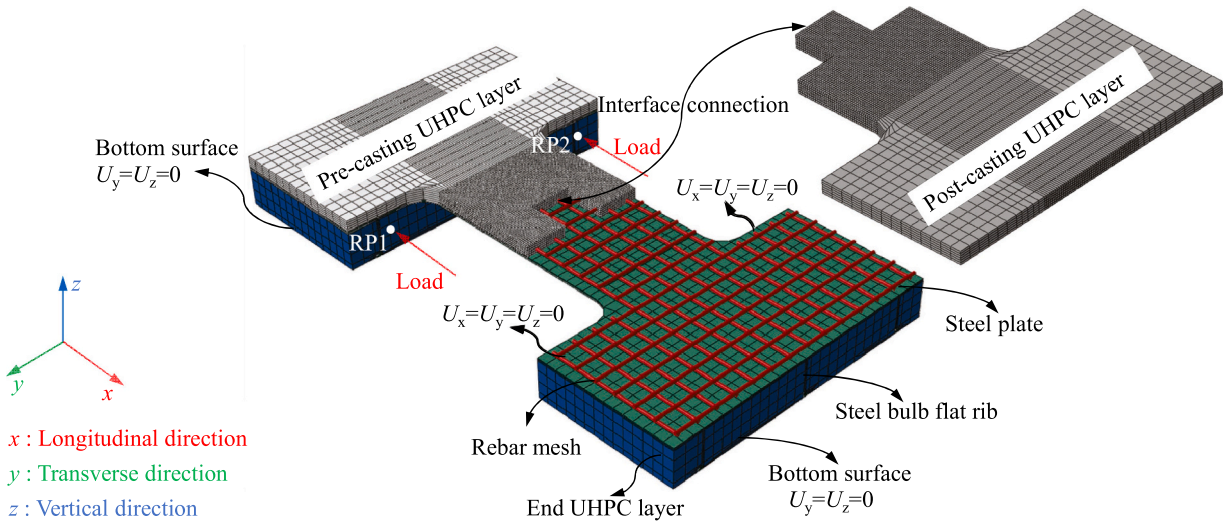

Fig. 9. Finite element model.

of the test. There are 5–7 localized cracks developed at the tested composite deck specimen matter with UHPC joint or not. The colored lines denote the developed thin cracks at stage II, and these cracks became invisible with the evolution of the localized cracks at stage III. The localized crack at the continuous UHPC zone for specimen SN-3 was distributed much denser than for specimen SN-2, demonstrating the increase in reinforcement contributes to reducing the crack spacing.

The localized crack comparison between the interface and the continuous UHPC is shown in Fig. 8(d). The fractured surface at the continuous UHPC was relatively coarse and was filled with evenly distributed pulled-out steel fibers. Whereas, the fractured surface at the interface was flat with a limited number of steel fibers. The fracture of the interface can be regarded as a brittle failure, which depends on the bond properties of the pre-/post-casting UHPC interface. The methods for handling pre-/post-casting UHPC interface roughness by wire brush still cannot make up for the weaknesses of the discontinuous UHPC matrix and discontinuous and sparse steel fibers at the interface, making the interface the weakest zone at tension. According to the first-cracking load P_{cr1}, as shown in Fig. 6(d), the tensile bond strengths of the pre-/post-casting UHPC interface were calculated to be 3.6 MPa and 4.7 MPa for specimen SN-2 and SN-3, respectively.

The two raptured rebars of specimen SN-2 are shown in Fig. 8(e). The two rebars were located at the same localized crack at the continuous casting zone. The phenomenon of why the rapture of rebar emerged at

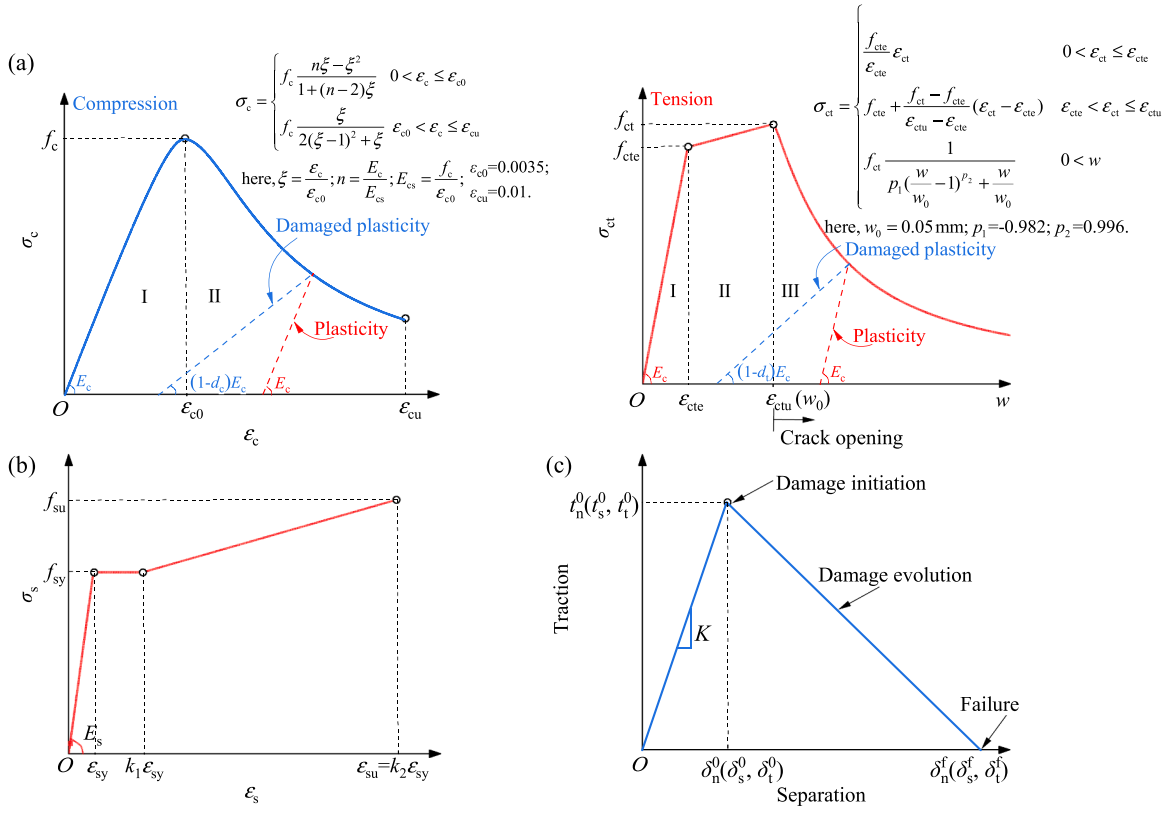

Fig. 10. Material constitutive models: (a) UHPC; (b) steel; and (c) traction-separation law for cohesive zone model.

Table 5
The plasticity parameters of CDP model for UHPC [32].

Parameter	Value	Explanation
ψ	54°	Dilation angle
e	0.1	Flow potential eccentricity
f_{b0}/f_{c0}	1.07	The ratio of initial equibiaxial compressive yield stress to initial uniaxial compressive yield stress
k_c	0.666	The coefficient determining the shape of the deviatoric cross-section
μ	0.0001	Viscosity parameter

the continuous UHPC zone and not at the interfaces, can be explained by the fiber distribution and the energy consumption mechanism contributed by fiber debonding from the UHPC matrix. The fiber-debonding has become the predominant tensile contribution once steel rebar yields, which intensifies the crack opening widening for the UHPC matrix and stress concentration for the corresponding rebars. The aggravating effect at the cracks in the continuous UHPC is more significant than that at the interface due to the more densely distributed and continuous steel fibers, making the rebars at the continuous UHPC zone more prone to be tensioned to fracture.

3. Numerical simulation

3.1. FEM scheme

To further investigate the cracking behavior of the segmented-casting UHPC joint in the steel-UHPC composite bridge deck, a finite element model (FEM) was developed and validated against the test results. Fig. 9 shows the established FEM of the tested specimens using ABAQUS, which is capable of simulating the nonlinear behavior of concrete material. The explicit solver was adopted to save computing time.

The solid element C3D8R, a three-dimensional eight-node reduced integration element, was chosen to simulate the UHPC layer and the steel bulb flat rib. The three-dimensional four-node reduced integration shell element S4R was used to model the flat steel plate. The three-dimensional two-node truss element T3D2 was selected to model the steel rebar, which was simulated to be embedded in the UHPC layer. As demonstrated in the measured elongation of the UHPC layer and the steel plate, the welded stud connectors provided an effective connection for the two components. Therefore, the connection between the UHPC layer and the steel plate was simulated by ties.

A global mesh size of 50 mm is used for the FEM, and the influence of mesh size on the FEM results will be analyzed in Section 3.4. It should be noted that the nodes at the pre-/post-casting UHPC interface should be aligned when meshing. Thus, the relative longitudinal displacement of the adjacent nodes can be adopted to simulate the cracking opening displacement at the interface.

To be consistent with the experimental loading and boundary conditions, the degrees of freedom (DOFs), U_y and U_z, of the bottom surface for the two enlarged two ends were restricted. The DOFs, U_x, U_y, and U_z, of the surface perpendicular to the x direction for one of the enlarged ends were restricted. The displacements of points RP1 and RP2 are linked to the displacements of the corresponding loading surfaces at the other enlarged end. This allowed the total force exerted by the hydraulic jacks to be monitored during displacement control.

3.2. Material modelling

As shown in Fig. 10(a), the compressive constitutive model of UHPC was referred to Yang's work[30], and the tensile constitutive model of UHPC was according to the formulation proposed by Gao et al. [31]. The compressive strength f_c and elastic modulus E_c, as well as the elastic tensile strength f_{cr}, the tensile strength f_{ct}, and the tensile strain at tensile strength ε_{ctu}, adopted this material test results, as listed in Table 4. The concrete damaged-plasticity (CDP) model in ABAQUS was adopted to simulate the continuous compression/tension damage of the UHPC layer. The basic parameters of the CDP model were according to existing research on UHPC [32], as listed in Table 5. The tensile damage variable d_t and the compressive damage variable d_c according to Kadhim et al. [33], as expressed in Eq.(1) and Eq.(2), respectively.

A tri-linear constitutive model, as shown in Fig. 10(b), was adopted to simulate the tensile properties of steel rebar and steel plate. The elastic modulus E_s, the yielding strength f_{sy}, the tensile strength f_{su}, and the yielding strain ε_{sy} were according to this material test values, as shown in Table 2. In addition, based on the material test results, the factor k_1 was set as 10 for both the steel rebar and the steel plate, and the factors k_2 of 40 and 100 were adopted for the steel rebar and the steel plate, respectively.

$$d_t = 1 - \frac{\sigma_{ct}}{f_{ct}} \tag{1}$$

$$d_c = 1 - \frac{\sigma_c}{f_c} \tag{2}$$

3.3. Interface modelling

Three methods to simulate the pre-/post-casting UHPC interface, the unbonded case, the perfectly bonded case, and the cohesive bonded case (between unbonded and perfectly bonded cases), were compared and validated against the test results. The schematic diagram of the three simulating methods is shown in Fig. 11.

(a) The unbonded case. The two nodes of the pre-casting and the post-casting UHPC layers at the interface had identical coordinates, but without any connection between the two nodes. Hence, the crack opening displacement of the interface can be calculated as the relative longitudinal deformation of the two nodes with identical coordinates.

(b) The cohesive case. The modelling method and crack opening calculating method were the same as the unbonded case. The only difference was the interface was simulated using a cohesive zone model (CZM) [34–36] which is characterized by the traction-separation law

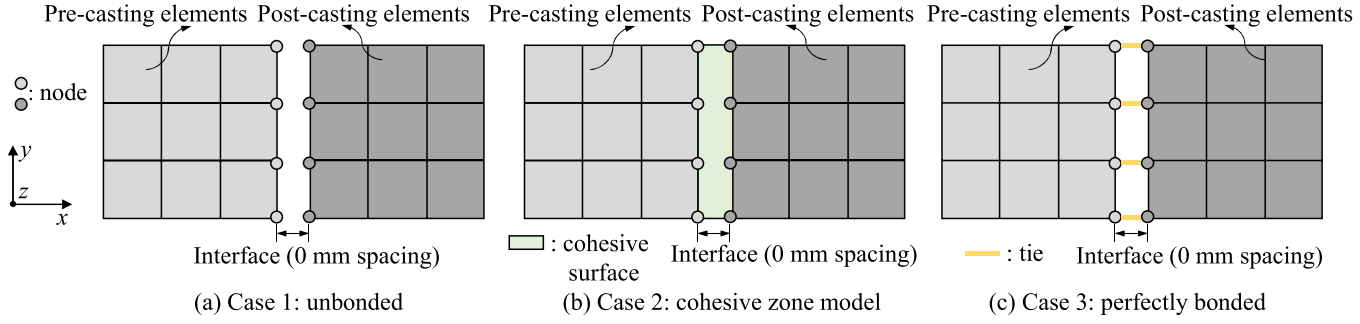

Fig. 11. Simulations methods for interface: (a) unbonded; (b) cohesive zone model; and (c) perfectly bonded.

Table 6
Parameters for cohesive bond properties [17,19].

Elastic stiffness (N/mm^3)		Bond strength (MPa)		Total displacement (mm)	Stabilization
K_{nn}	K_{ss}, K_{tt}	t_n^0	t_s^0, t_t^0	δ_n^f, δ_s^f, δ_t^f	0.001
147.67	20358	4.32	5.63	0.6	

shown in Fig. 10(c).

The CZM contains three traction-separation relations, one normal direction (n) perpendicular to the interaction plane, and two tangential directions (s and t) parallel to the interaction plane [37]. It assumes a linear elastic behavior up to the bond strength (t_n^0, t_s^0, t_t^0), followed by the damage initiation at the peak and damage evolution at the post-peak stage, until reaching the final failure at the maximum separations (δ_n^f, δ_s^f, δ_t^f). In this study, the damage initiation criterion, as expressed in Eq. (3), was adopted. The symbol $\langle\rangle$ denotes the Macaulay bracket, which signifies that compression would not initiate damage. Hence, if $t_n > 0$ (tension), $\langle t_n\rangle = t_n$, and $\langle t_n\rangle = 0$ otherwise.

$$\left(\frac{\langle t_n\rangle}{t_n^0}\right)^2 + \left(\frac{t_s}{t_s^0}\right)^2 + \left(\frac{t_t}{t_t^0}\right)^2 = 1 \tag{3}$$

A proper traction-separation law is the principal parameter for simulating the cracking and crack opening development for the interface. The traction-separation relationship in tension for UHPC-UHPC interface [17], and the corresponding relation in shear for UHPC-HSC (high-strength concrete)[19], were adopted in this study. The related cohesive parameters are listed in Table 6.

(c) The perfectly bonded case. The extreme case for the interface is the pre-casting and the post-casting UHPC layers are firmly connected without tension fracture. In this case, the boundary surfaces of the pre-casting and the post-casting UHPC layers were simulated by ties in ABAQUS. Therefore, no crack opening of the interface will be obtained.

3.4. Mesh dependence

The FEM load-elongation curves from mesh sizes of 50 mm, 20 mm, and 10 mm for the UHPC layer located between the two enlarged ends

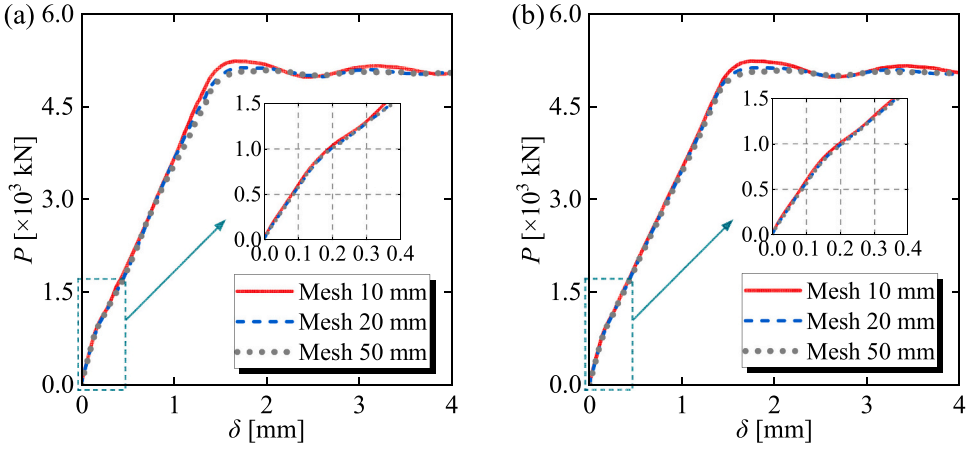

Fig. 12. Axial load-elongation response of FEM from different mesh sizes for specimen SN-2: (a) the UHPC layer; and (b) the steel plate.

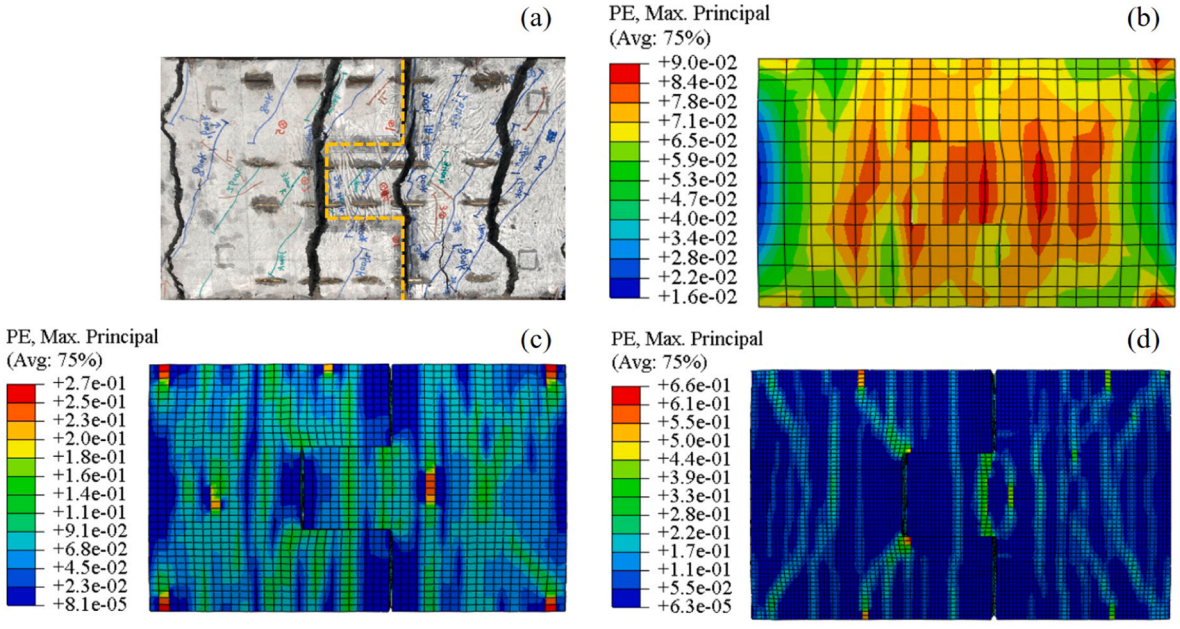

Fig. 13. Ultimate crack distribution comparison between test and FEM for specimen SN-2: (a) test result; (b) FEM with a mesh size of 50 mm; (c) FEM with a mesh size of 20 mm; and (d) FEM with a mesh size of 10 mm.

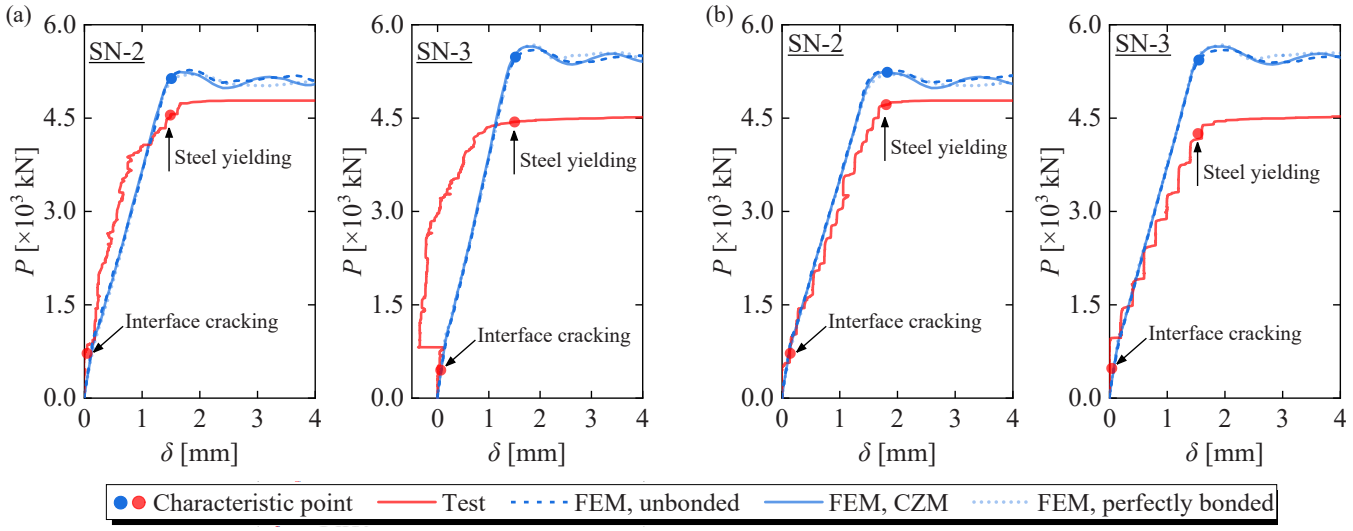

Fig. 14. Comparison of interface modelling methods on axial load-elongation response: (a) the UHPC layer; and (b) the steel plate.

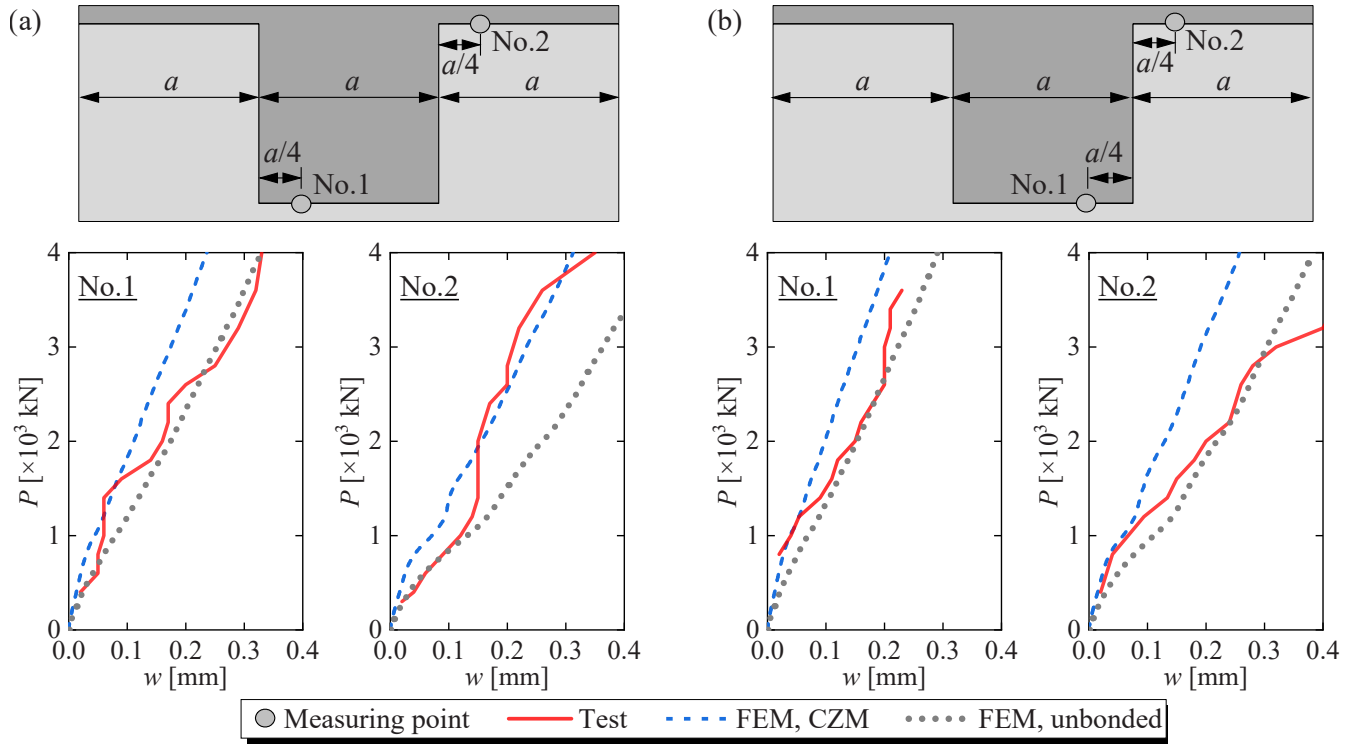

Fig. 15. Comparison of interface modelling methods on crack opening development: (a) SN-2; and (b) SN-3.

are compared, as shown in Fig. 12. The CZM model was used to simulate the pre-/post-casting UHPC interface in this comparison. It can be observed that the investigated mesh sizes have a negligible influence on the load-elongation responses of the UHPC layer as well as the steel plate.

The ultimate crack distribution comparison between FEM from the investigated mesh sizes and the test is shown in Fig. 13. The CDP model in ABAQUS assumed that cracking initiates at a point when the tensile equivalent plastic strain is greater than zero, and the maximum principal plastic strain is positive [38]. Therefore, the maximum principal plastic strain was chosen to characterize the cracking in FEM. As compared, the crack distribution of FEM from a mesh size of 10 mm showed the best agreement with the test. Hence, the mesh size of 10 mm was chosen for the UHPC layer in the following FEMs.

3.5. Numerical results

3.5.1. Numerical validation

The comparison of the interface modelling methods on the axial load-elongation response is shown in Fig. 14, and also validated against the test response. The FEM curves almost coincided with each other, indicating the investigated interface modelling methods have an insignificant influence on the global tensile response for the tested specimen. As has been demonstrated in the test result, the UHPC joint has a negligible influence on the load-bearing capacity of the composite deck. Moreover, the FEM curve agrees well with the test curve for specimen

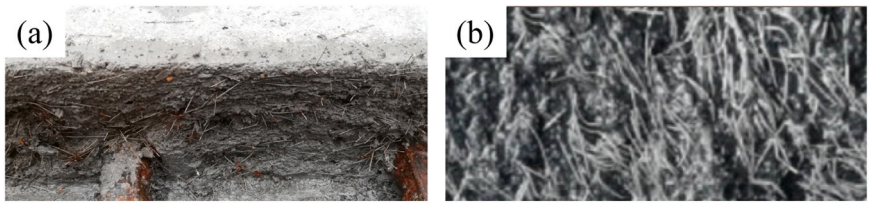

Fig. 16. UHPC-UHPC interfaces handled by: (a) wire brush (this study); and (b) high-pressure water jet [17].

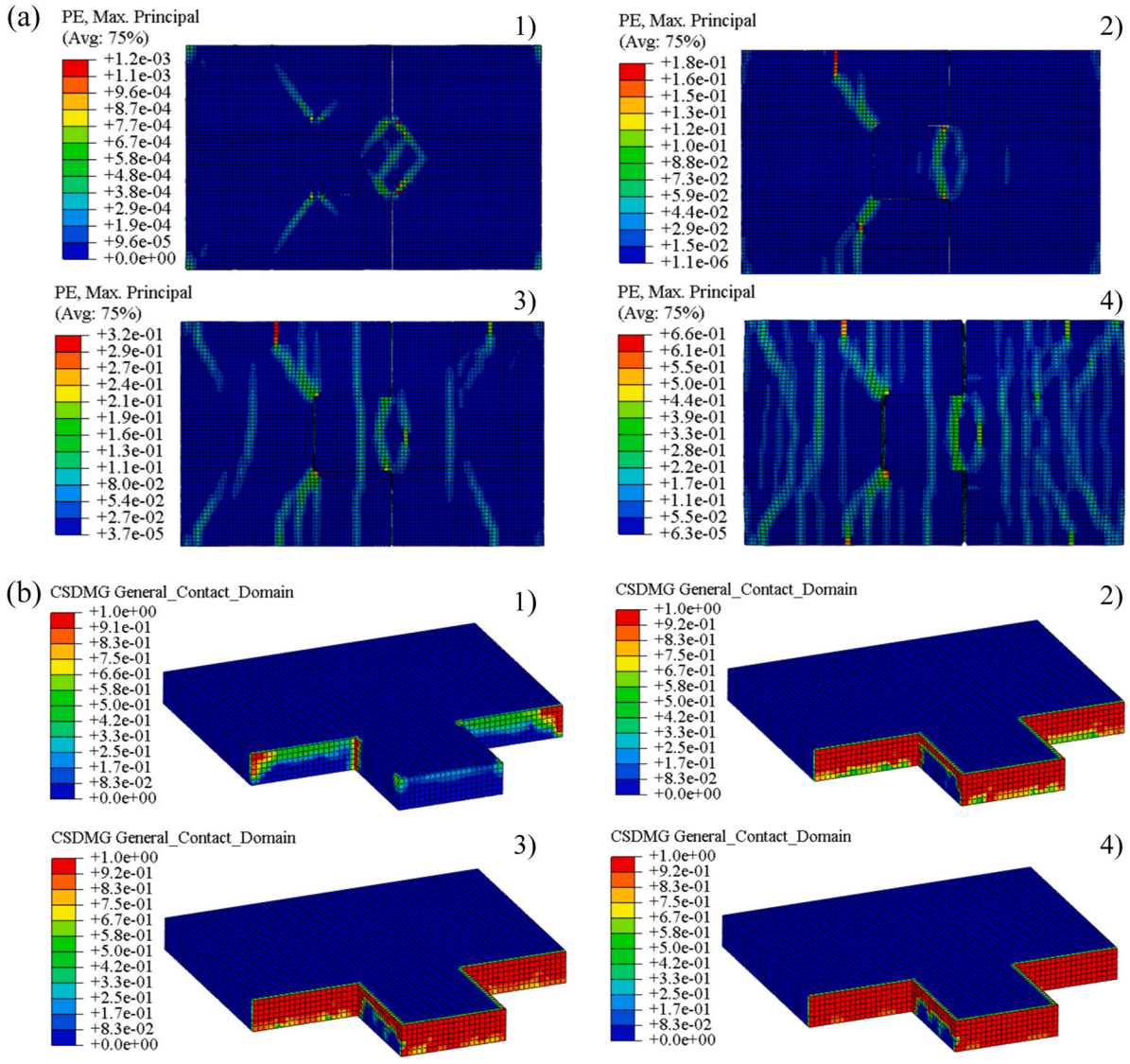

Fig. 17. Damage evolution: (a) Cracking development of UHPC layer; and (b) stiffness degradation of cohesive interface.

SN-2. As explained in Section2.2.1, the test result of specimen SN-3 should have a larger yielding capacity than specimen SN-2 owing to the higher reinforcement ratio, while a lower yielding capacity was obtained due to the greater dispersion brought by only one specimen. While this error will not be induced in FEM, which is featured by more ideal conditions on both material properties and loading or boundary conditions. From this view, the agreement between FEM and test for specimen SN-3 is considered sufficient.

Fig. 15 compares the crack opening development for the interface modelling methods. Generally, the FEM with CZM resulted in smaller crack openings compared to the FEM with the unbonded interface and the test crack opening is located between the results of these two FEMs. The unbonded method neglects the bond contribution of the pre-/post-casting UHPC interface, overestimating the real crack opening at the interface. The FEM results of the CZM are determined by the bond properties which are closely related to the techniques for handling the interface roughness. The adopted CZM properties in FEM were obtained for the UHPC-UHPC interface [17] handled by the high-pressure water jet. Fig. 16 compares the UHPC interface between this study using the wire brush and Feng et al. [17] adopting the high-pressure water jet. It is obvious the high-pressure water jet enables a much coarser interface and larger numbers of exposed steel fibers, which contributed to more excellent bond properties. Hence, the FEM with CZM using the bond parameters referred to Feng et al., yielded an underestimated result for

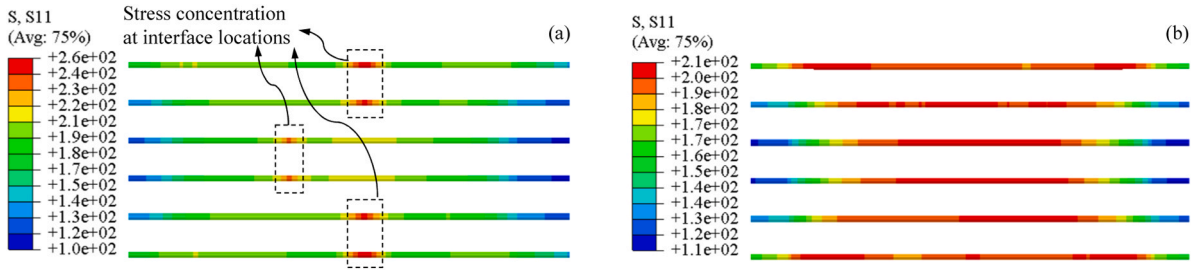

Fig. 18. Tensile stress distribution of longitudinal rebars at $P = 2500$ kN: (a) specimen SN-2 with joint; and (b) specimen SN-1 without joint.

Table 7
Parameters of the supplementary models.

Type	Case	Parameters
CZM	Bond strength kt_n^0	k = 0.6, 0.8, **1.0**, 1.2, 1.4
	Equivalent CZM	UHPC material
	Failure displacement $k\delta_n^f$	k = **1**,2,4,6,8,10
Rebar quantity	Reinforcement ratio ρ_s	ρ_s = 0, 1.7 %, **3.4 %**, 5.0 %, 6.7 %, 8.4 %
Joint shape	Inclined angle α	$\alpha = 0°, \pm 6°, \pm 14°$, **90°**
	Fillet radius r	r = 30 mm, 50 mm, 70 mm, **without**

Note: The bold number indicates the benchmark parameter of the physically tested specimens, and the bold CZM is referred to Table 6.

the crack opening at the interface. This also demonstrates the importance of a proper bond property for CZM to simulate the cracking performance of the interface.

Considering the different physical mechanisms of the CZM and unbonded method, the CZM was adopted to investigate the cracking behavior of the pre-/post-casting UHPC interface in the following FEMs. Because no related bond properties test results for the interface polished by the wire brush have been reported, the bond properties listed in Table 6 will be continuously adopted for CZM.

3.5.2. Discussions

The cracking development of the UHPC layer with a segmented-casting joint, by means of showing the maximum principal strain distributions, is illustrated in Fig. 17(a). As shown, the first cracking originated from the intersection of the interfaces, followed by the penetration of cracks throughout the joint section. Then, cracks initiated and developed at the continuous casting UHPC zone coupled with the widening of the crack opening at the interface. The simulated damage process showed good agreement with the experimental observations.

Fig. 17(b) presents the CSDMG (Scalar Stiffness Degradation for Cohesive Surfaces) evolution of the interface. The damage initiated at the corners of the interface, then extended toward the center of the sub-interfaces as the loading increased.

Fig. 18 plots the tensile stress distribution of the longitudinal rebars for specimens SN-1 and SN-2 under load of 2500 kN, which was approximately 0.6 times the yielding load. The stress distribution for specimen SN-1 was relatively uniform, while stress concentration developed at the interface locations for specimen SN-2. The occurrence of rebar fracture at the interfaces in FEM was inconsistent with the experimental observation, where rebar ruptured within the continuous casting UHPC zone. A possible explanation is that in the CZM the interface was essentially modeled as a localized crack once reaching the bond strength. In the continuous UHPC layer, the cracks are modeled as smeared cracks, with a possible overestimated tension stiffening effect of the UHPC. However, the debonding and pullout of steel fibers from the UHPC matrix at cracks in the continuous UHPC layer, which leads to the rebar fracture, cannot be achieved in this FEM. Despite some modelling errors, the FEM effectively simulated the tensile response of the composite deck and the crack opening development at the joint.

4. Parametric study

Based on the validated FEM, a supplementary parametric analysis of the cracking behavior of the segmented UHPC joint in a steel-UHPC composite deck was conducted. Table 7 lists the investigated parameters, including the CZM, the reinforcement ratio, and the joint shape. The CZM consisted of two cases: the varying bond strengths and failure displacements. The joint shape was composed of varying inclined angles and fillet radiuses.

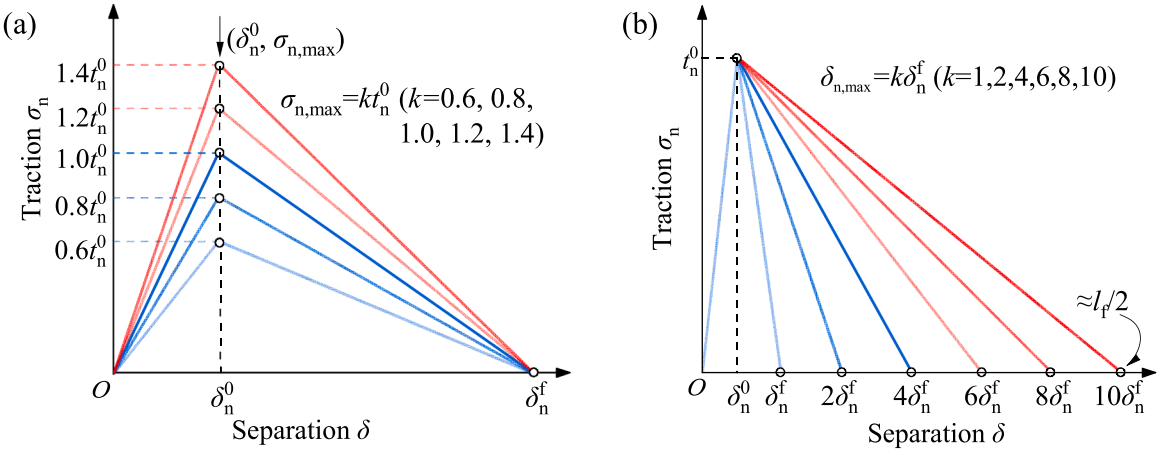

Fig. 19. Varying cohesive zone models: (a) varying bond strengths; and (b) varying failure displacements.

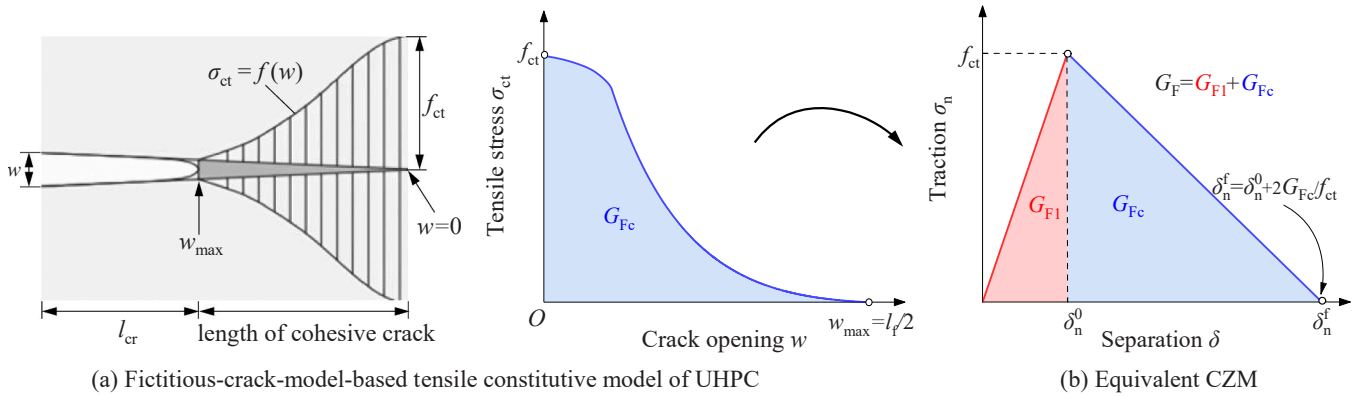

(a) Fictitious-crack-model-based tensile constitutive model of UHPC (b) Equivalent CZM

Fig. 20. Equivalent cohesive zone model from the tensile constitutive model of UHPC.

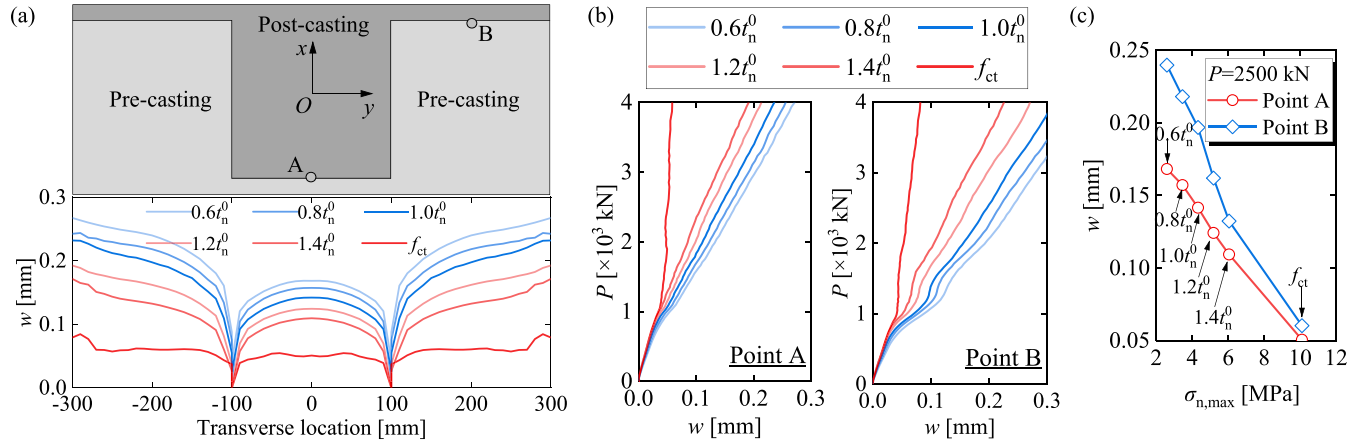

Fig. 21. Influence of bond strength on crack opening displacement at the interface: (a) crack opening distribution under $P = 2500$ kN; (b) axial load-crack opening displacement response; and (c) crack opening displacement-bond strength relation.

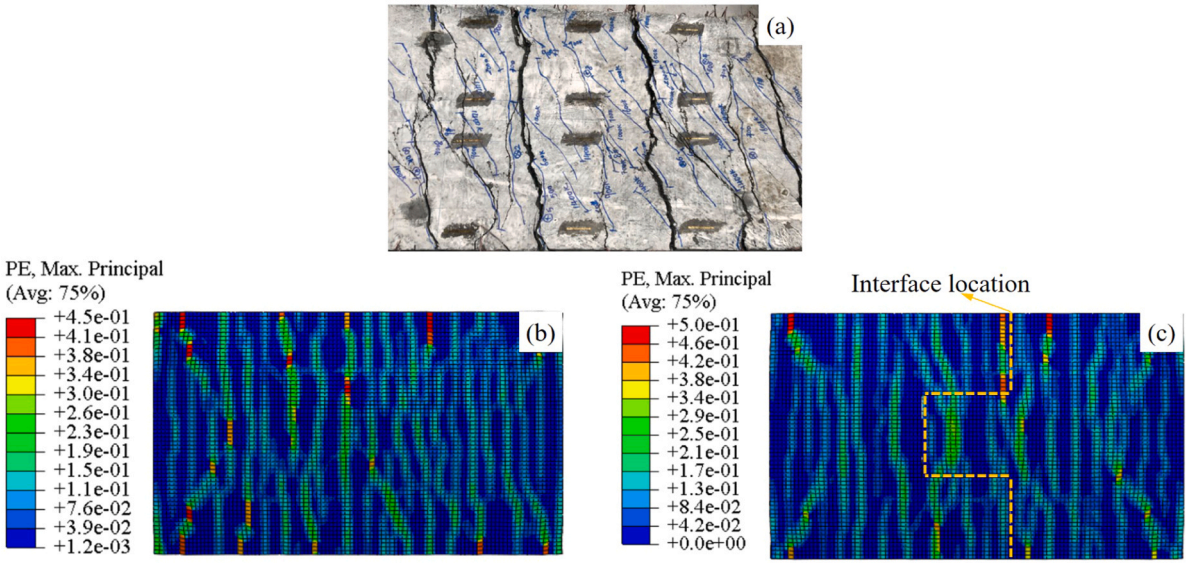

Fig. 22. Cracking pattern comparison between test and FEM: (a) specimen SN-1; (b) FEM of continuous UHPC layer; and (c) FEM with joint using the equivalent CZM.

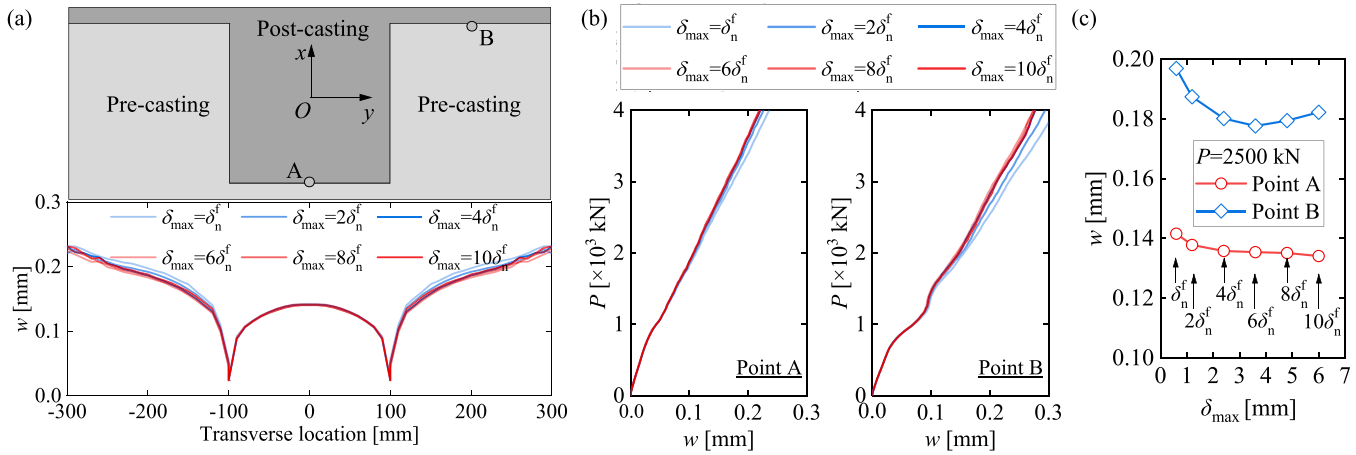

Fig. 23. Influence of failure displacement on crack opening displacement at the interface: (a) crack opening distribution under $P = 2500$ kN; (b) axial load-crack opening displacement response; and (c) crack opening displacement-failure displacement relation.

4.1. Cohesive zone model

4.1.1. Case 1: varying bond strengths and equivalent CZM from constitutive model of UHPC

Fig. 19(a) shows the CZMs with varying bond strengths, where the displacements were fixed. The bond properties of the pre-/post-casting UHPC interface are weaker than the constitutive properties of UHPC material due to the discontinuities in both the UHPC matrix and the steel fibers. The interface can be regarded as the continuous UHPC material when the bond properties are equal to the constitutive properties of UHPC material, and this will be the ideal case for the interface. The fictitious-crack-model-based[39] tensile constitutive model of UHPC can be equivalent to the CZM, as illustrated in Fig. 20. In this equivalent CZM, the normal bond strength t_n^0 is the tensile strength f_{ct} of UHPC, and the failure displacement δ_n^f changes with the fracture energy G_{Fc} of UHPC which is expressed as the area enclosed by the tensile strength and the crack opening displacement. It should be noted that only the normal bond properties were varying while the tangent bond properties were fixed, due to the fact that the former has a more significant impact on the crack opening at the interface.

Fig. 21 presents the influence of the bond strength of CZM on the crack opening at the interface, in which f_{ct} denotes the equivalent CZM from the tensile constitutive model of UHPC. Overall, the crack opening at the interface along the transverse direction presented a butterfly-shaped distribution. The cracking opening displacement at the interface intersection was equal to zero, and increased along the transverse direction. Two middle points at the central interface and at one of the side interfaces respectively, points A and B, were selected to quantify the influence of the investigated parameter on the crack opening displacement (also applicable to subsequent parameter studies).

In general, the crack opening displacement decreases with the increase of bond strength. Specifically, as the bond strength increased from $0.6t_n^0$ to $1.4t_n^0$, the crack openings of points A and B decreased by 54 % and 45 %, respectively. The FEM with equivalent CZM from the tensile constitutive model of UHPC led to the minimum crack opening displacement, compared with other CZM with varying bond strengths. Moreover, the cracking opening displacements of the equivalent CZM along the interface were less than 0.1 mm under $P = 2500$ kN.

Fig. 22 compares the cracking patterns of the continuous UHPC layer and of the segmented UHPC layer with the joint simulated by the equivalent CZM. The FEM with joint simulated by the equivalent CZM presented a similar cracking pattern with the FEM for continuous UHPC layer, which has been effectively validated against the tested cracking pattern of specimen SN-1. This demonstrates once the material constitutive model of UHPC is adopted in CZM, the interface can be considered as a continuous casting UHPC layer.

4.1.2. Case 2: varying failure displacements

Fig. 19(b) shows the CZMs with varying failure displacements, where the bond strength t_n^0 was fixed. Fig. 23 presents the influence of the failure displacement of CZM on the crack opening displacement at the interface. Generally, the crack opening displacement diminished as the failure displacement increased. Specifically, as the failure displacement escalated from δ_n^f to $10\delta_n^f$, the crack opening displacements at points A and B decreased by slight margins of 5.3 % and 7.5 %, respectively.

Compared to the simulating results of bond strengths, it can be concluded that improving the bond strength yields a more significant effect on reducing the crack opening displacement than increasing the

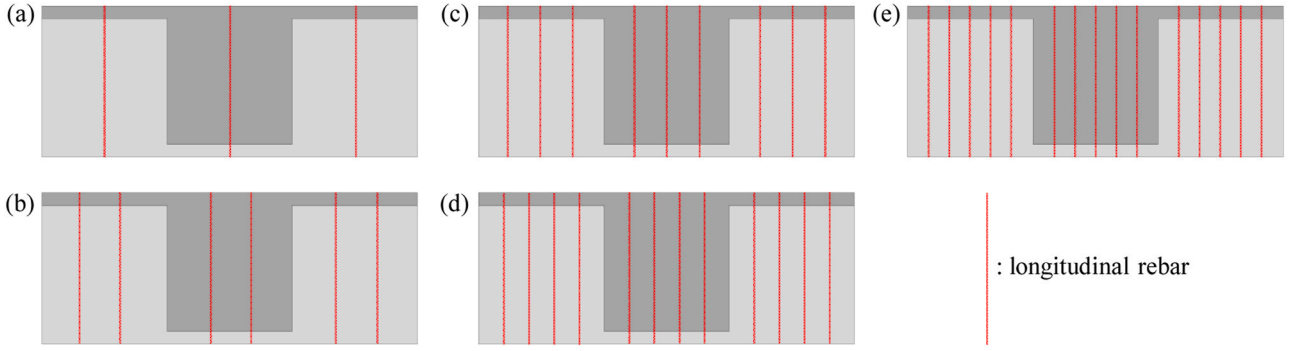

Fig. 24. Varying reinforcement ratios: (a) $n = 3$, $\rho_s = 1.7$ %; (b) $n = 6$, $\rho_s = 3.4$ %; (c) $n = 9$, $\rho_s = 5.0$ %; (d) $n = 12$, $\rho_s = 6.7$ %; and (e) $n = 15$, $\rho_s = 8.4$ %.

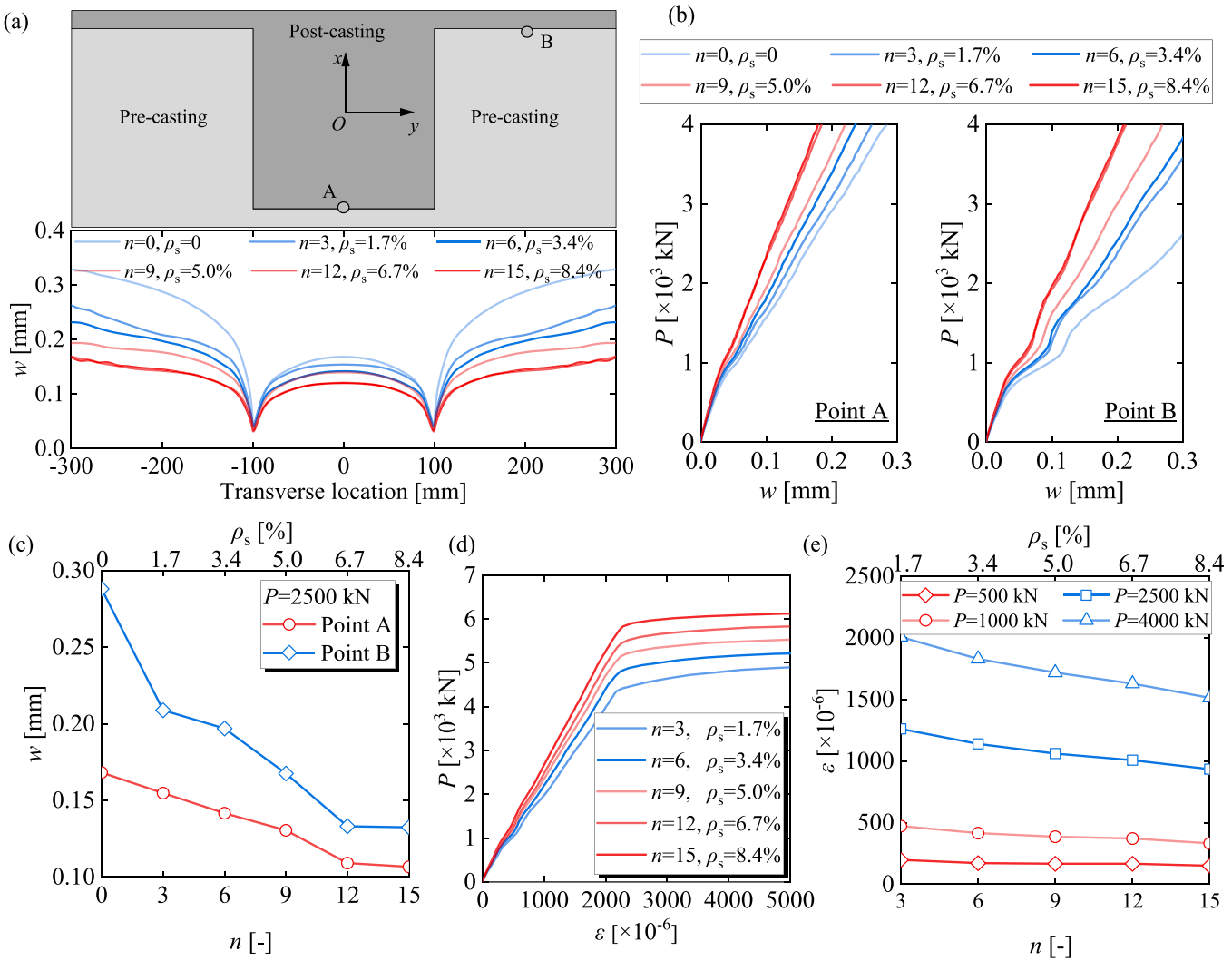

Fig. 25. Influence of reinforcement ratios on crack opening displacement at the interface: (a) crack opening distribution under $P = 2500$ kN; (b) axial load-crack opening displacement response; (c) crack opening displacement-reinforcement ratio relation; (d) axial load-average rebar strain response; and (e) average rebar strain-reinforcement ratio relation.

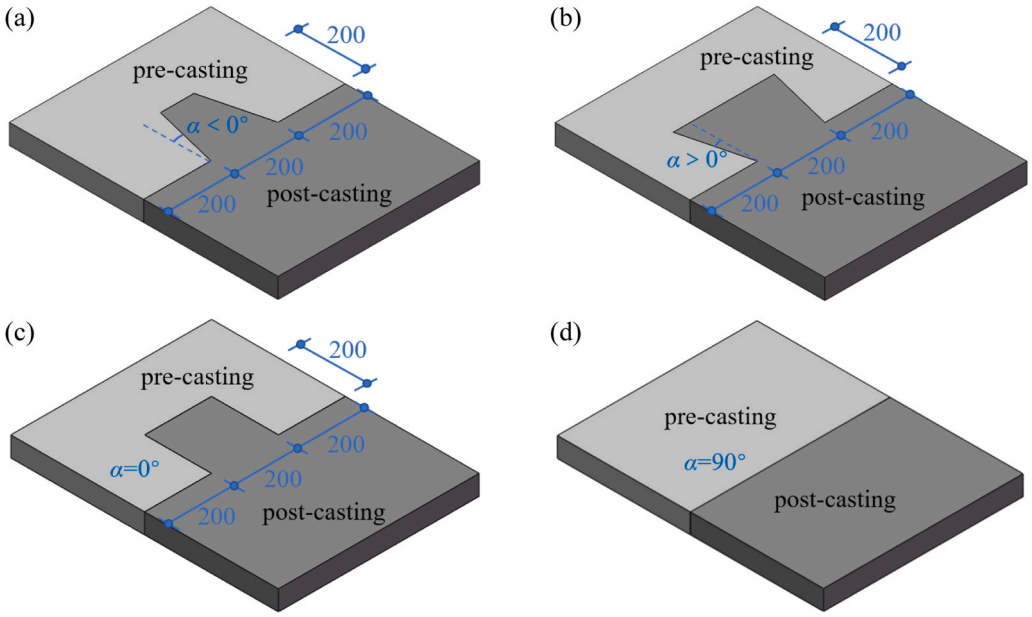

Fig. 26. Varying inclined angles: (a) $\alpha < 0°$; (b) $\alpha > 0°$; (c) $\alpha = 0°$; and (d) $\alpha = 90°$.

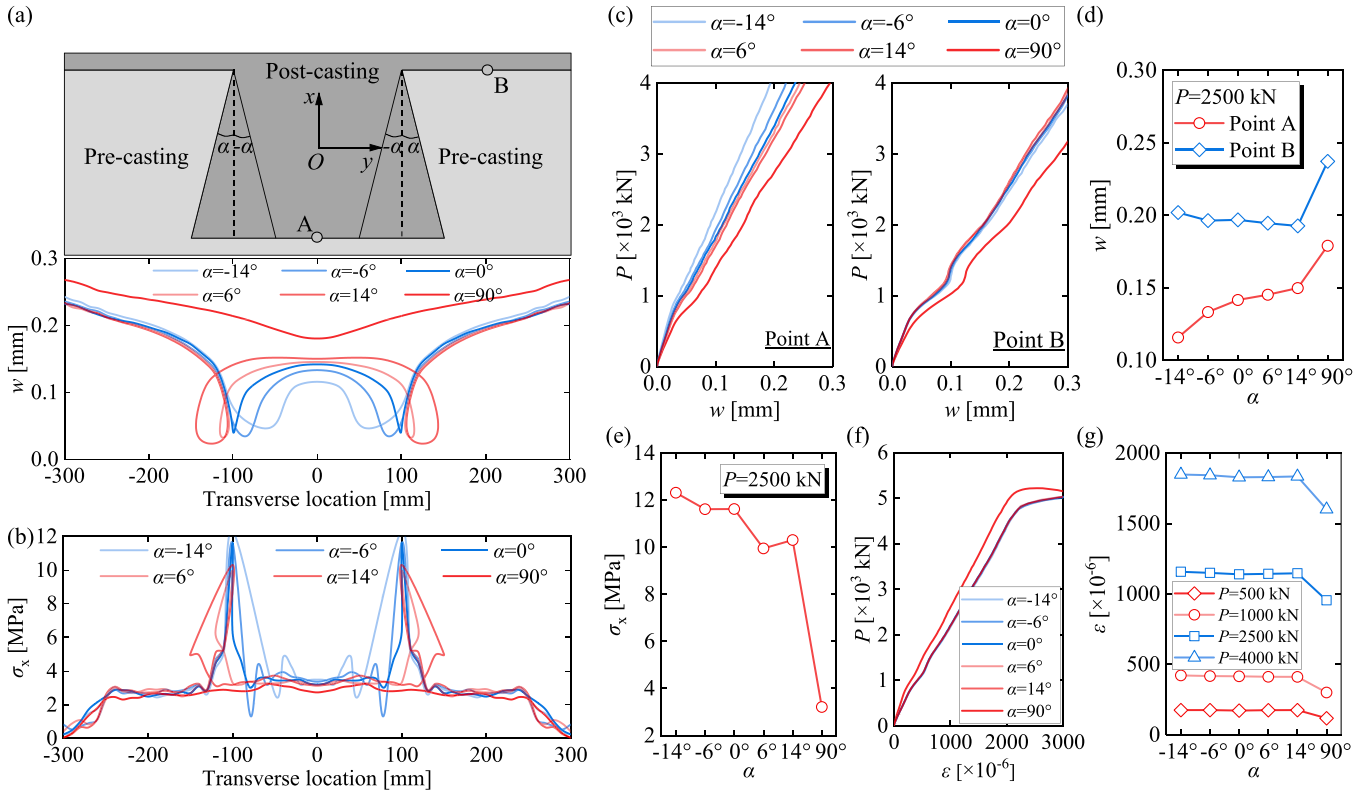

Fig. 27. Influence of inclined angles on crack opening displacement at the interface: (a) crack opening distribution under $P = 2500$ kN; (b) longitudinal normal stress distribution at the interface under $P = 2500$ kN; (c) axial load-crack opening displacement response; (d) crack opening displacement-inclined angle relation; (e) longitudinal normal stress-fillet radius relation at the interface intersection; (f) axial load-average rebar strain response; and (g) average rebar strain-inclined angle relation.

failure displacement of the CZM. Given that the bond strength is contingent upon interface roughness [16,40], and the failure displacement is primarily dictated by exposed steel fibers at the interface, it is imperative to prioritize enhancing the UHPC matrix roughness at the interface during the interface treating process.

4.2. Reinforcement ratios

Fig. 24 presents the varying longitudinal rebar arrangements and the related reinforcement ratios, where the diameter of the rebar was fixed at 16 mm. The influence of reinforcement ratios on crack opening

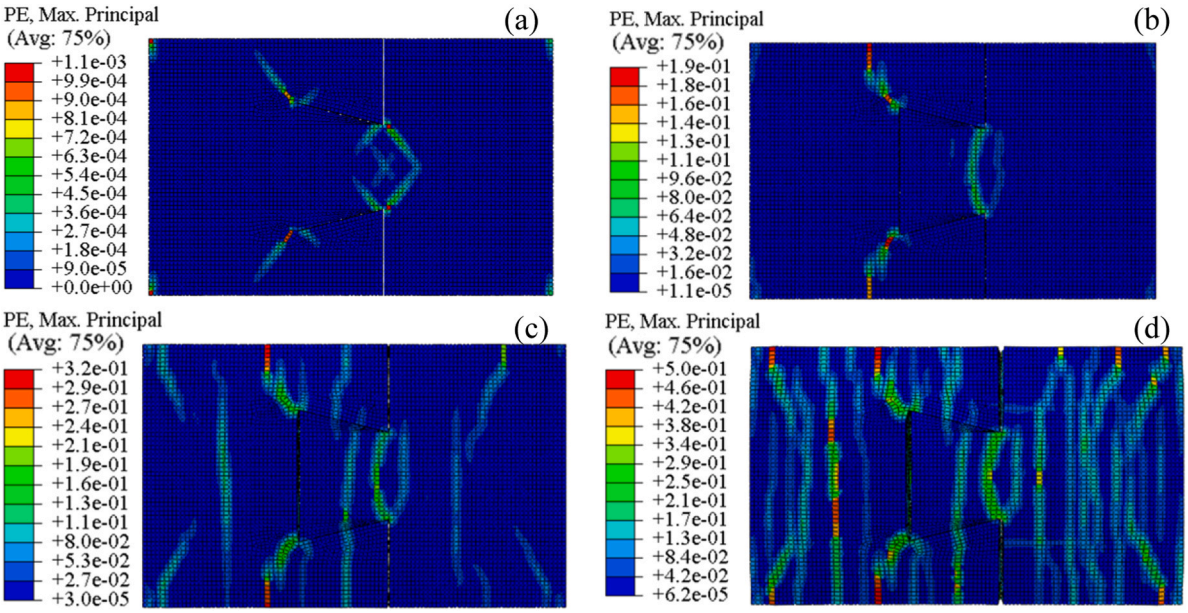

Fig. 28. Crack distribution of UHPC layer with 14°-shape joint at elongation of: (a) 0.4 mm; (b) 10 mm; (c) 21 mm; and (d) 70 mm.

displacement and average rebar strain is shown in Fig. 25. The average rebar strain represents the mean value of the tensile strain observed in longitudinal rebars at the interface.

Generally, the crack opening displacement decreased as the reinforcement ratio increased. Specifically, as the reinforcement ratio has grown from 0 to 6.7 %, the crack opening displacements at points A and B presented a relatively stable decrease with a maximum drop rate of 13 % and 27 %, respectively. Whereas, the crack opening displacement exhibited a negligible decrease as the reinforcement ratio increased from 6.7 % to 8.4 %. By comparison, the average rebar strain exhibited a stable drop as the rebar quantity increased from 0 to 15. Considering the construction convenience, the reinforcement ratios of 5.0 % and 6.7 %, corresponding to rebar spacings of 50 mm and 40 mm respectively with 16-mm rebar are suggested. The proposed rebar arrangement takes into account both construction feasibility and durability, ensuring that the crack opening displacement remains below 0.2 mm when subjected to 60 % of the yielding load.

4.3. Joint shapes

4.3.1. Case 1: varying inclined angles

Fig. 26 presents the schematic diagram of the joints with varying inclined angles. The influence of the inclined angles on crack opening displacement, normal stress at the interface, and the average rebar strain is shown in Fig. 27. As for the crack opening displacement, the inclined angle of 90°, i.e. the straight joint, has the largest crack opening displacement compared to with other angles, and this should be forbidden in application. The inclined angle presents a negligible

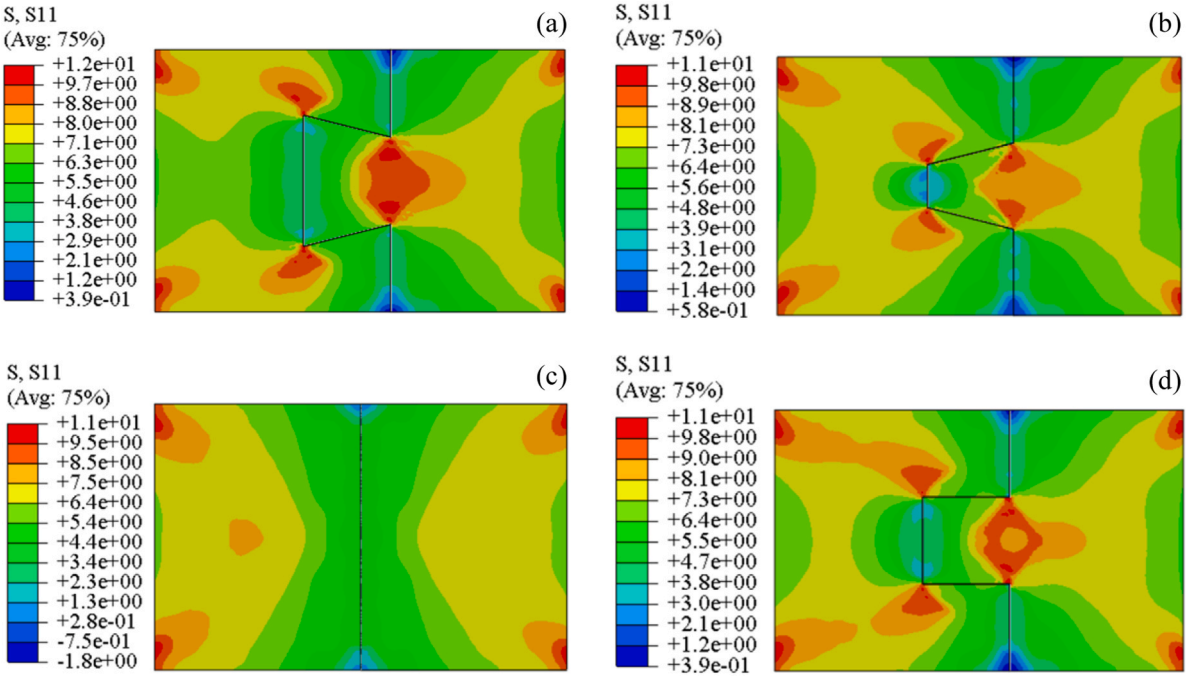

Fig. 29. Longitudinal normal stress distribution of the UHPC layer at $P = 2500$ kN: (a) $\alpha = 14°$; (b) $\alpha = -14°$; (c) $\alpha = 0°$; and (d) $\alpha = 90°$.

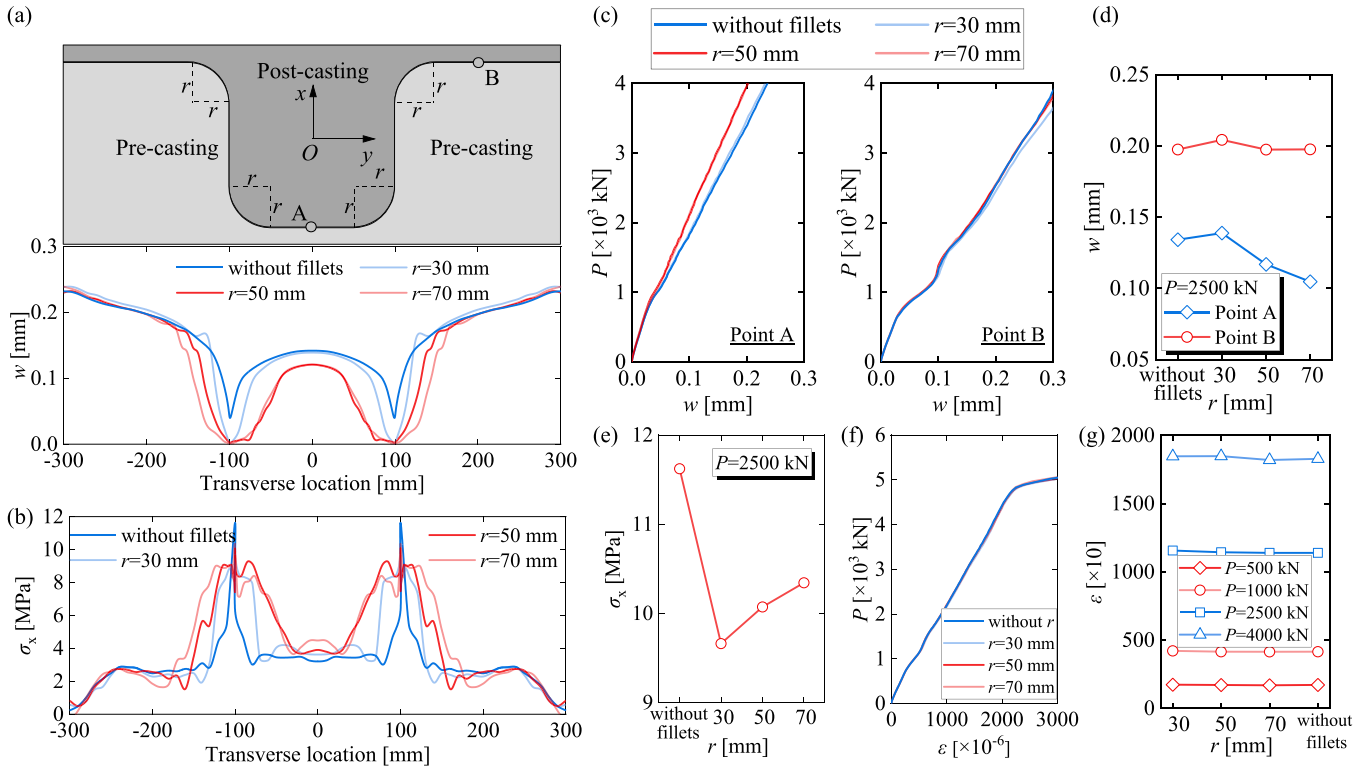

Fig. 30. Influence of fillet radius on crack opening displacement at the interface: (a) crack opening distribution under $P = 2500$ kN; (b) longitudinal normal stress distribution at the interface under $P = 2500$ kN; (c) axial load-crack opening displacement response; (d) crack opening displacement-fillet radius relation; (e) longitudinal normal stress-fillet radius relation at the interface intersection; (f) axial load-average rebar strain response; and (g) average rebar strain-fillet radius relation.

influence on the crack opening displacement of point B. The crack opening displacement of point A decreased by 22 % and increased by 6 % as the angle changed from 0° to − 14°, and changed from 0° to 14°, respectively. In addition, the inclined angle exhibited a negligible effect on the average rebar strain.

It is considered that the 14°-shape should perform better crack resistance than − 14°-shape due to the mechanical interlocking. One point to ensure the mechanical interlocking is that the two parts on both sides of the interfaces should be continuous and complete components. But when these shapes are used in UHPC joint, cracks initiate at the interface intersections and propagate though the transversal direction under tension. Therefore, the protruding zone of the inclined joints is cut

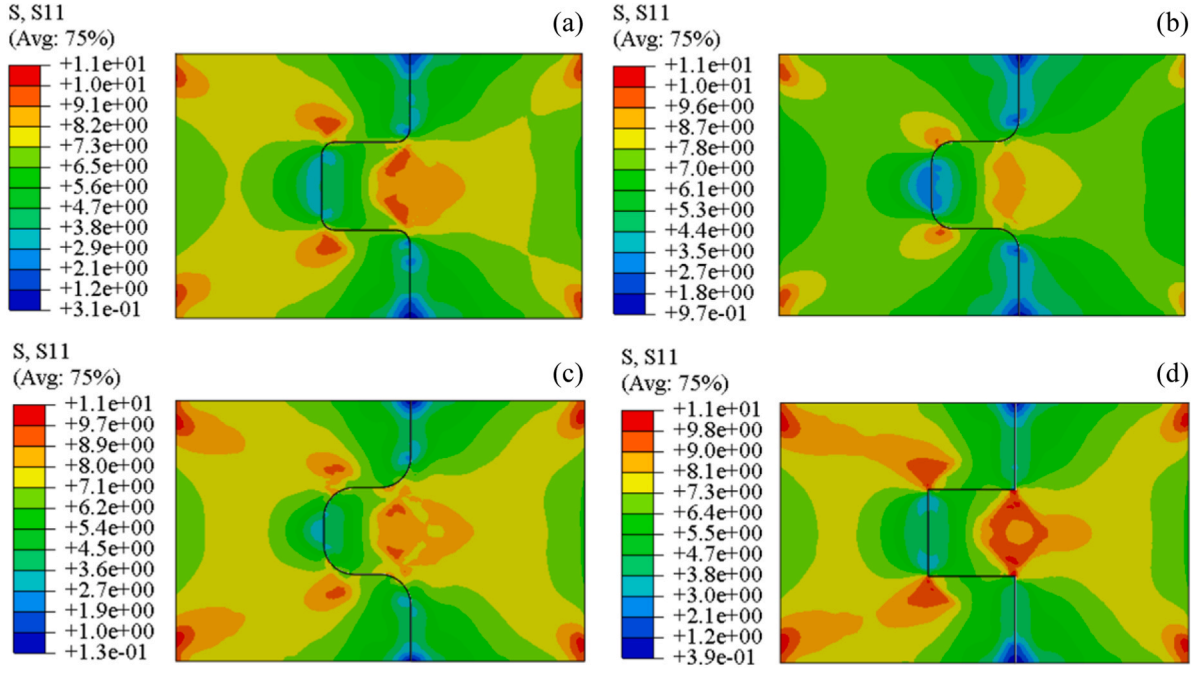

Fig. 31. Longitudinal normal stress distribution of the UHPC layer at $P = 2500$ kN: (a) $r = 30$ mm; (b) $r = 50$ mm; (c) $r = 70$ mm; and (d) without fillet.

off by the transverse through cracks at the interface, thus being isolated from the continuous casting UHPC zone, as shown in Fig. 28. Hence, the mechanical interlocking effect cannot be exerted. The crack resistance at the interface predominantly depends on the area of the continuous-casting cross-section at the interface section. The 14°-shape has a smaller continuous-casting cross-section than the -14^0-shape, thus leading to a larger crack opening.

The maximum normal tensile stress of the interface was located at the intersection of interfaces, varying between 10.0 MPa and 12.3 MPa with a varying inclined angle from − 14° to 14°. Fig. 29 plots the longitudinal normal stress distribution cloud of the UHPC joint. Stress concentration developed at the intersection of interfaces except for the inclined angle of 90°. Comprehensively considering the convenience of mold making for joint, and the durability of limiting the crack opening to 0.2 mm under 60 % of the yielding load, the rectangular joint with an inclined angle of 0° is suggested for engineering practice.

4.3.2. *Case 2: varying fillet radii*

The shape of the rectangular joint was further optimized to reduce the stress concentration by introducing the fillet at the intersection. Fig. 30 presents the influence of varying fillet radii of 30 mm, 50 mm, and 70 mm on crack opening, normal stress at the interface, and the average rebar strain. It should be noted that the investigated fillet radiuses were designed based on the interface size of 200 mm.

The investigated fillet radius has a negligible impact on the crack opening displacement, with values ranging from 0.10 mm to 0.13 mm for point A and from 0.19 mm to 0.20 mm for point B, respectively. Additionally, the influence of the fillet radius on the average rebar strain can be disregarded. The normal tensile stresses at the interface intersections for fillet radii of 30 mm, 50 mm, 70 mm, and without fillet were 9.66 MPa, 10.07 MPa, 10.34 MPa, and 11.62 MPa. It can be observed that the fillet is beneficial for reducing the normal tensile stress, and the difference from the investigated fillet radii has a slight impact.

Fig. 31 plots the longitudinal normal stress distribution cloud of the UHPC joint. It is observed that the fillet radius of 50 mm has the least stress-concentration-affected zone. Considering the minimum normal tensile stress at the interface intersections and the least stress-concentration-affected zone at the interface intersection, a fillet radius of 50 mm is recommended in construction applications.

5. Conclusions

Based on the above investigations, the main conclusions are:

(1) The failure process of the steel-UHPC composite bridge deck system under direct tension initiates with cracking at the pre-/post-casting UHPC interface, followed by multi-cracking within the continuous casting UHPC zone. Subsequently, yielding occurs in the steel rebar and steel plate, coupled with localized cracking in the UHPC layer. The steel fibers/matrix debonding at the continuous casting UHPC zone intensifies stress concentration in the rebar, ultimately leading to tension fracture.

(2) The tension failure of the segmented UHPC joint exhibits brittleness, with a wire-brush-treated interface bond strength typically ranging from approximately 3 to 5 MPa. Additionally, the UHPC joint has an insignificant impact on the load-bearing capacity of the composite bridge deck system.

(3) The numerical model, incorporating a CZM to simulate the interface, effectively characterized the crack initiation and propagation of the interface as well as the evolution of tensile damage of the UHPC layer. Improving the bond strength of the CZM has a more pronounced effect on reducing the crack opening at the interface than increasing the failure displacement. It is crucial to prioritize enhancing the interface roughness over increasing the exposure of steel fibers at the interface to control the cracking of the UHPC joint.

(4) The reinforcement ratio has a significant effect on controlling the crack opening displacement at the interface. It is recommended to adopt reinforcement ratios of 5.0 % and 6.7 %, corresponding to rebar spacings of 50 mm and 40 mm, respectively, using 16-mm rebar for this UHPC joint.

(5) The utilization of a flat joint shape is prohibited in the composite bridge deck system. The mechanical interlocking of inclined joints cannot be achieved because the protruding zone is cut off from the continuous casting UHPC zone by the transverse through cracks at the interface. Taking into account factors such as the ease of mold making, durability to restrict crack opening displacement to 0.2 mm, and minimizing stress concentration, the rectangular joint with an optimized 50-mm fillet radius at the intersection is suggested to be adopted in this investigated joint.

CRediT authorship contribution statement

Debao Chen: Software. **Max Hendriks:** Writing – review & editing, Supervision, Methodology. **Zhanchong Shi:** Writing – review & editing, Writing – original draft, Software, Methodology, Investigation, Formal analysis, Conceptualization. **Qingtian Su:** Writing – review & editing, Supervision, Project administration, Funding acquisition. **Wei Xie:** Software, Investigation, Formal analysis.

Declaration of Competing Interest

The authors declare that they have no known competing financial interests or personal relationships that could have appeared to influence the work reported in this paper.

Data Availability

Data will be made available on request.

Acknowledgements

The financial support provided by the Fujian Transportation Science and Technology Project (Grant NO.202126) is greatly appreciated by the authors. The first author also acknowledges the financial support of the China Scholarship Council (Grant NO. 202006260216).

References

[1] Wolchuk R. Lessons from weld cracks in orthotropic decks on three european bridges. J Struct Eng 1990;116:75–84. https://doi.org/10.1061/(ASCE)0733-9445(1990)116:1(75).
[2] Shi Z, Su Q, Kavoura F, Veljkovic M. Behavior of short-headed stud connectors in orthotropic steel-UHPC composite bridge deck under fatigue loading. Int J Fatigue 2022;160:106845. https://doi.org/10.1016/j.ijfatigue.2022.106845.
[3] Wolchuk R. Steel orthotropic decks: developments in the 1990s. Transp Res Rec 1999;1688:30–7. https://doi.org/10.3141/1688-04.
[4] Walter R, Olesen JF, Stang H, Vejrum T. Analysis of an orthotropic deck stiffened with a cement-based overlay. J Bridge Eng 2007;12:350–63. https://doi.org/10.1061/(ASCE)1084-0702(2007)12:3(350).
[5] Teixeira De Freitas S, Kolstein H, Bijlaard F. Fatigue assessment of full-scale retrofitted orthotropic bridge decks. J Bridge Eng 2017;22:04017092. https://doi.org/10.1061/(ASCE)BE.1943-5592.0001115.
[6] Wolchuk R. Structural Behaviour of Surfacings on Steel Orthotropic Decks and Considerations for Practical Design. Struct Eng Int 2002;12:124–9. https://doi.org/10.2749/101686602777965586.
[7] Pan W-H, Fan J-S, Nie J-G, Hu J-H, Cui J-F. Experimental study on tensile behavior of wet joints in a prefabricated composite deck system composed of orthotropic steel deck and ultrathin reactive-powder concrete layer. J Bridge Eng 2016;21:04016064. https://doi.org/10.1061/(ASCE)BE.1943-5592.0000935.
[8] Shao X, Yi D, Huang Z, Zhao H, Chen B, Liu M. Basic performance of the composite deck system composed of orthotropic steel deck and ultrathin RPC layer. J Bridge Eng 2013;18:417–28. https://doi.org/10.1061/(ASCE)BE.1943-5592.0000348.
[9] Dieng L, Marchand P, Gomes F, Tessier C, Toutlemonde F. Use of UHPFRC overlay to reduce stresses in orthotropic steel decks. J Constr Steel Res 2013;89:30–41. https://doi.org/10.1016/j.jcsr.2013.06.006.

[10] Graybeal B, Brühwiler E, Kim B-S, Toutlemonde F, Voo YL, Zaghi A. International perspective on UHPC in bridge engineering. J Bridge Eng 2020;25:04020094.
[11] Huang B-T, Zhu J-X, Weng K-F, Li VC, Dai J-G. Ultra-high-strength engineered/strain-hardening cementitious composites (ECC/SHCC): material design and effect of fiber hybridization. Cem Concr Compos 2022;129:104464.
[12] Zhu J-X, Weng K-F, Huang B-T, Xu L-Y, Dai J-G. Ultra-high-strength engineered cementitious composites (UHS-ECC) panel reinforced with FRP bar/grid: development and flexural performance. Eng Struct 2024;302:117193.
[13] Cao J, Shao X, Deng L, Gan Y. Static and fatigue behavior of short-headed studs embedded in a thin ultrahigh-performance concrete layer. J Bridge Eng 2017;22:04017005. https://doi.org/10.1061/(ASCE)BE.1943-5592.0001031.
[14] Zhang S, Shao X, Cao J, Cui J, Hu J, Deng L. Fatigue performance of a lightweight composite bridge deck with open ribs. J Bridge Eng 2016;21:04016039. https://doi.org/10.1061/(ASCE)BE.1943-5592.0000905.
[15] Shao C, Yan H, Chen L, Xu Y, Cao S. Widening and strengthening of the Songpu bridge. Struct Eng Int 2019;29:354–61.
[16] Hussein HH, Walsh KK, Sargand SM, Steinberg EP. Interfacial properties of ultrahigh-performance concrete and high-strength concrete bridge connections. J Mater Civ Eng 2016;28:04015208. https://doi.org/10.1061/(ASCE)MT.1943-5533.0001456.
[17] Feng Z, Li C, Li H, Zhou J, Pan R, Liu G. Interfacial bond performance of ultrahigh performance concrete wet joints. J Chin Ceram Soc 2021;49:2393–404.
[18] Lu K, Pang Z, Xu Q, Yao Y, Wang J, Miao C. Bond strength between substrate and post-cast UHPC with innovative interface treatment. Cem Concr Compos 2022;133:104691. https://doi.org/10.1016/j.cemconcomp.2022.104691.
[19] Hussein HH, Walsh KK, Sargand SM, Al Rikabi FT, Steinberg EP. Modeling the shear connection in adjacent box-beam bridges with ultrahigh-performance concrete joints. I: model calibration and validation. J Bridge Eng 2017;22:04017043. https://doi.org/10.1061/(ASCE)BE.1943-5592.0001070.
[20] Qi J, Bao Y, Wang J, Li L, Li W. Flexural behavior of an innovative dovetail UHPC joint in composite bridges under negative bending moment. Eng Struct 2019;200:109716.
[21] Qi J, Cheng Z, Wang J, Zhu Y, Li W. Full-scale testing on the flexural behavior of an innovative dovetail UHPC joint of composite bridges. Struct Eng Mech 2020;75:49–57.
[22] Qiu M, Shao X, Yan B, Zhu Y, Chen Y. Flexural behavior of UHPC joints for precast UHPC deck slabs. Eng Struct 2022;251:113422. https://doi.org/10.1016/j.engstruct.2021.113422.
[23] Zhao C, Wang K, Zhou Q, Deng K, Cui B. Full-scale test and simulation on flexural behavior of dovetail-shaped reactive powder–concrete wet joint in a composite deck system. J Bridge Eng 2018;23:04018051. https://doi.org/10.1061/(ASCE)BE.1943-5592.0001265.
[24] Chen D, Zeng M, Su Q, Lou Y. Research on interfacial treatment measures of wet joints in composite bridge deck composed of steel and UHPC layer. China J Highw Transp 2018;31:154–62.
[25] Shao X., Hu J., Liang Z., Li C., Xiang J. DB43/T 1173—2016 Technical Specification for Steel-STC Lightweight Composite Structure Deck. Changsha, China: Hunan Provincial Bureau of Quality and Technical Supervision; n.d.
[26] SAC/TC183. GB / T228–2002 Metallic materials-Tensile testing at ambient temperature. Beijing, China: General Administration of Quality Supervision, Inspection and Quarantine of the People's Republic of China; 2002.
[27] Dalian University of Technology. Standard test methods for fiber reinforced concrete. Beijing, China: China Planning Press,; 2010.
[28] Bian C, Wang J-Y. Mechanical and damage mechanisms of reinforced ultra high performance concrete under tensile loading. Constr Build Mater 2019;226:259–79. https://doi.org/10.1016/j.conbuildmat.2019.07.162.
[29] Shi Z, Liang M, Su Q, Kanstad T, Ferrara L. Tensile behavior of rebar-reinforced coarse aggregate ultra-high performance concrete (R-CA-UHPC) members: Experiments and restrained shrinkage creep effect. Cem Concr Compos 2024;151:105574. https://doi.org/10.1016/j.cemconcomp.2024.105574.
[30] Yang J. Flexural behaviour of ultra-high performance concrete beams prestressed with CFRP tendons. Doctoral thesis. Hunan University,; 2007.
[31] Gao X, Wang J, Guo J, Liu C. Axial tensile mechanical properties and constitutive relation model of ultra-high performance concrete under cyclic loading. Acta Mater Compos Sin 2021;38:3925–38.
[32] Krahl PA, Carrazedo R, El Debs MK. Mechanical damage evolution in UHPFRC: experimental and numerical investigation. Eng Struct 2018;170:63–77. https://doi.org/10.1016/j.engstruct.2018.05.064.
[33] Kadhim MMA, Saleh AR, Cunningham LS, Semendary AA. Numerical investigation of non-shear-reinforced UHPC hybrid flat slabs subject to punching shear. Eng Struct 2021;241:112444. https://doi.org/10.1016/j.engstruct.2021.112444.
[34] Shojaei A, Shao J. Porous rock fracture mechanics: with application to hydraulic fracturing, drilling and structural engineering. Woodhead Publishing,; 2017.
[35] Rozylo P, Debski H. Stability and load-carrying capacity of short composite Z-profiles under eccentric compression. Thin-Walled Struct 2020;157:107019.
[36] Rozylo P. Failure phenomenon of compressed thin-walled composite columns with top-hat cross-section for three laminate lay-ups. Compos Struct 2023;304:116381.
[37] Hibbitt, Karlsson, Sorensen. Abaqus/CAE User's Manual. Hibbitt, Karlsson & Sorensen, Incorporated; 2002.
[38] Lubliner J, Oliver J, Oller S, Oñate E. A plastic-damage model for concrete. Int J Solids Struct 1989;25:299–326. https://doi.org/10.1016/0020-7683(89)90050-4.
[39] Hillerborg A, Modéer M, Petersson P-E. Analysis of crack formation and crack growth in concrete by means of fracture mechanics and finite elements. Cem Concr Res 1976;6:773–81. https://doi.org/10.1016/0008-8846(76)90007-7.
[40] Qiu M, Sun Y, Qian Y. Interfacial bonding performance of 3D-printed Ultra-High Performance Strain-Hardening Cementitious Composites (UHP-SHCC) and cast normal concrete. J Build Eng 2024;82:108268.